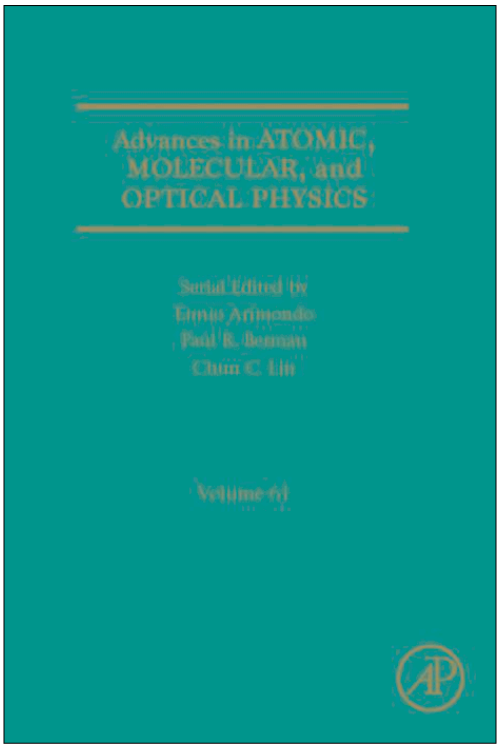

From Ergin H. Ahmed, The Autler–Townes Effect in Molecules: Observations, Theory, and Applications. In: E. Arimondo, P. R. Berman, C. C. Lin, editor, Advances in Atomic, Molecular, and Optical Physics. Chennai: Inc.; 2012. p 467-514.
ISBN: 978-0-12-396482-3

CHAPTER 9

The Autler–Townes Effect in Molecules: Observations, Theory, and Applications

Ergin H. Ahmed[a], **John Huennekens**[b], **Teodora Kirova**[c], **Jianbing Qi**[d], and **A. Marjatta Lyyra**[a]

[a] *Department of Physics, Temple University, Philadelphia, PA 19122, USA*
[b] *Department of Physics, Lehigh University, Bethlehem, PA 18015, USA*
[c] *National Institute for Theoretical Physics (NITheP), Stellenbosch 7600, South Africa*
[d] *Department of Physics and Astronomy, Penn State University, Berks Campus, Reading, PA 19610, USA*

Contents

Advances in Atomic, Molecular, and Optical Physics, Volume 61, Copyright © 2012 Elsevier Inc.
ISSN 1049-250X, http://dx.doi.org/10.1016/B978-0-12-396482-3.00009-0.

Abstract

In recent years experimental investigations in the field of quantum optics have expanded from atomic to molecular systems despite orders of magnitude weaker oscillator strengths and complex relaxation pathways in molecules that represented serious challenges in the past. The richness of molecular excitation pathways and the variety of molecules has made it possible to develop novel high resolution spectroscopic applications of various quantum optics tools. The present work discusses spectroscopic investigations of several diatomic alkali molecules based on the Autler–Townes effect created by application of a "strong" continuous wave coupling laser field. We demonstrate how the Autler–Townes effect can be used to control molecular angular momentum alignment. We also show that the Autler–Townes split line shape, combined with accurate measurement of the coupling laser electric field amplitude, can be used to determine absolute magnitudes of the electronic transition dipole moment matrix elements. These in turn can be used to map out the internuclear distance dependence of the electronic transition dipole moment function $\mu_e(R)$. For weaker electronic transitions this method, combined with calibrated and normalized intensity measurements, makes it possible to overcome the traditional systematic complications associated with emission line strength and lifetime measurements. The former only yields a relative transition moment function and the latter frequently involves more than one transition dipole moment function. We also demonstrate that the electric field amplitude in the coupling laser Rabi frequency can be used as a "tuning" mechanism for the mixing coefficients of molecular energy levels that are weakly perturbed by the spin–orbit interaction. This makes it possible to use the Autler–Townes effect to control the valence electron spin polarization, i.e., the spin multiplicity of some molecular quantum states.

1. INTRODUCTION

1.1 Coherent Phenomena

Studies of the interactions of coherent light with matter have resulted in the discovery of many intriguing coherent phenomena, and have led to numerous important and useful applications in a wide variety of fields.

The underlying effect in many of these phenomena is the so-called Autler–Townes (AT) effect (Autler & Townes, 1955) (also known as the AC- or dynamic Stark shift), which is characterized by the appearance of a double peak structure in the atomic/molecular states under the action of an oscillating electric field of a laser. The AT doublet is created by the strong control laser field that couples the atomic or molecular levels, and the separation of the doublet components is proportional to the Rabi frequency $\Omega = \mu E/\hbar$. Here μ is the transition dipole matrix element and E is the laser electric field amplitude. AT is usually observed in the absorption spectra of a probe laser as its frequency is scanned. The AT effect has been extensively studied in atoms (Delsart & Keller, 1976; Gray & Stroud, 1978; Knight & Milonni, 1980; Picque & Pinard, 1976). More recently, it has also been examined in a few experiments involving molecular systems, mainly for spectroscopic applications and for the measurements of transition dipole moments and lifetimes of highly excited molecular states (Atherton et al., 1986; Garcia-Fernandez et al., 2005; Qi et al., 1999, Qi et al., 2002; Quesada et al., 1987). In addition, it has been used for all-optical control of the angular momentum alignment of nonpolar molecules (Qi et al., 1999), for quantum control via the Nonresonant Dynamic Stark Effect (NRDSE) (Sussman et al., 2005; Sussman et al., 2006 Underwood et al., 2003), and for Selective Population of Dressed States (SPODS) (Wollenhaupt et al., 2005; Wollenhaupt et al., 2006a; Wollenhaupt et al., 2006b). More complex systems, in which the AT based coherent phenomena have been observed, include quantum dots (Muller et al., 2007; Vamivakas et al., 2009; Xu et al., 2007) and superconducting qubits (Baur et al., 2009; Sillanpää et al., 2009).

One of the coherent phenomena based on the AT effect is Electromagnetically Induced Transparency (EIT) (Boller et al., 1991; Harris, 1997; Harris et al., 1990) which is caused by the destructive quantum interference between different excitation pathways leading to reduction or full cancellation of transition probabilities. The first investigation of the coherent interference leading to a cancellation of absorption was performed by Fano (1961). There the interference between two excitation channels to the continuum led either to suppression or to enhancement of photo-ionization. Harris et al. (1990) were the first to coin the term "EIT" to describe the process of rendering transparent an otherwise optically thick medium. A pair of dressed states (Cohen-Tannoudji & Reynaud, 1977), also called the AT doublet (Autler & Townes, 1955), plays the same role as the closely spaced Fano resonances. The excitation pathways associated with each of the dressed states can interfere destructively, so that the linear susceptibilities from the two components cancel out, leading to elimination of probe field absorption. It has been demonstrated that EIT manifests itself as a dip in fluorescence or in absorption as a function of the detuning of one of the fields when the other is fixed to resonance (Fulton et al., 1995; Ichimura

et al., 1998). The first demonstration of EIT was based on a Λ-type energy level system in Sr vapor (Boller et al., 1991).

Most EIT schemes utilize a Λ-, V-, or cascade-type excitation scheme (Boon et al., 1999). More complicated configurations including additional levels, such as the inverted-Y (Joshi & Xiao, 2003), N- (Han et al., 2005), and tripod-type (Karpa et al., 2008) configurations, have been studied in atomic systems. In the context of light storage (Joshi & Xiao, 2005), dark-state polaritons in a four-level inverted-Y scheme have been shown to be useful for two-channel quantum memory.

Recently, EIT has also been extended to solid state media. After its first observation in rare earth doped insulators (Turukhin et al., 2002), EIT has been demonstrated in quantum wells (Phillips et al., 2003), quantum dots (Xu et al., 2008) and in nitrogen-vacancy centers (Santori et al., 2006).

The investigation of quantum coherence phenomena in cold atoms has also attracted more attention recently. The advantage of using cold atoms as an EIT medium is due to the practical absence of Doppler broadening below mK temperatures, which allows for more flexible experimental arrangement of field polarizations and propagation directions. In addition, at such low temperatures the reduced collisional rates also minimize decoherence effects. Wang et al. (2004) report an experimental study of EIT in a multi-level cascade excitation scheme in cold ^{85}Rb atoms confined in a magneto-optical trap (MOT). Similarly, EIT with simultaneous coupling of multiple hyperfine structure components has been observed in a MOT (Kowalski et al., 2009).

The realization of EIT applications at low light field intensities has certain restrictions, which can be overcome by combining EIT and Rydberg gases. The strong interactions between highly excited Rydberg atoms greatly enhance the non-linear properties of the medium, opening up new possibilities for potential applications in quantum optics. Experiments involving EIT and coherent population trapping (CPT) in Rydberg gases have been reported (Mohapatra et al., 2008; Pritchard et al., 2010; Schempp et al., 2010), and theoretical models based on reduced-density matrix and Monte Carlo methods (Ates et al., 2011) have been used to investigate the effects of Rydberg–Rydberg interactions on the response of the medium, successfully reproducing experimental data (Sevincli et al., 2011).

Similar to EIT, the cancellation of absorption is observed in the processes of CPT and "dark" state creation (Alzetta et al., 1976; Arimondo, 1995; Arimondo & Orriols, 1976). In this case, a Λ-type system (two ground levels and an excited level), which is coupled by two laser fields, has an eigenstate which does not contain any excited state amplitude and is thus decoupled from interaction with the light fields. Population can be trapped indefinitely in this "dark" state via spontaneous decay from the upper state.

While the trapping of population in the phenomenon of CPT is achieved spectroscopically, e.g., via optical pumping, the "dark" state of the

Λ system can also be created by using a counter intuitive pulse sequence through the method of Stimulated Raman Adiabatic Passage (STIRAP) developed by Bergmann and coworkers (Bergmann et al., 1998; Kuklinski et al., 1989; Vitanov et al., 2001). During this process, a coupling field pulse in the Λ excitation scheme is turned on first, creating a "dark" state which is given by the initial ground state. After that, the strength of a second weak coupling field is gradually increased, while the first coupling field is simultaneously decreased in intensity so that the dark state evolves into the second ground level with a phase shift. In this manner, complete adiabatic transfer of population from the initially populated state to the final state without any population flow through the excited state is achieved. The only requirement in this process is that it proceed sufficiently slowly (adiabatic transfer) that the state vector can follow the rotation of the mixing angle.

Since STIRAP is not the main focus of this chapter, the reader is referred to the reviews (Bergmann et al., 1998; Vitanov et al., 2001) on this subject. We will only mention here the recent applications of STIRAP in the area of ultracold molecule production. The indirect methods for cooling molecules are based on creating ultracold molecules from already existing ultracold atomic samples via photoassociation or the Feshbach resonance technique. Sweeping a magnetic field over a Feshbach resonance of an atomic pair leads to a "magnetic association" into a weakly bound molecule. As a second step, the molecule is transferred to its ground rovibrational state by means of STIRAP. The efficiency of this technique is almost unity. It depends on the use of a favorable intermediate state, and a variety of homonuclear and heteronuclear molecules have been produced (Durr et al., 2004; Greiner et al., 2003; Ospelkaus et al., 2006; Regal et al., 2003; Voigt et al., 2009; Zwierlein et al., 2003). The production of ultracold KRb molecules in their absolute ground state has been achieved from a near quantum degenerate gas mixture in an optical dipole trap (Ni et al., 2008).

1.2 Coherent Phenomena in Molecules

Compared to atomic systems, the molecular energy level structure and relaxation mechanisms are much more complex. Each molecular electronic state consists of a multitude of rovibrational levels. Because each excited rovibrational level is coupled to a number of lower lying rovibrational levels in other electronic states by spontaneous decay or other relaxation mechanisms, the system is unavoidably "open." In contrast to an open system, a system is closed if the excitation and decay mechanisms do not involve energy levels beyond those that are needed for the observation of the coherence effect. In this sense, atoms can usually be considered examples of closed systems. These differences between open and closed systems

also require modifications in the theoretical models used to predict and simulate experimental results.

Molecular transition moments are also much smaller than atomic transition moments. Furthermore, due to the density of molecular energy levels, high spectral resolution is required in studies of molecular coherence effects. This complicates the experimental investigations, since the cw lasers required for high resolution generally provide weaker electric field amplitudes. Thus the resulting Rabi frequencies are smaller. In addition to their smaller magnitudes, the molecular Rabi frequencies fall short of matching or exceeding the residual Doppler linewidth. For all of these reasons, the emergence of applications of quantum optics using molecular systems has been delayed relative to those involving atomic coherence effects.

On the other hand a molecular system provides opportunities for a rich variety of excitation schemes. Therefore a single experimental apparatus allows one to study several coherence effects and their applications to quantum control in the frequency domain.

Some earlier experiments on AT splitting/AC-Stark shift in gas-phase molecules (Girard et al., 1983; Huo et al., 1985; Quesada et al., 1987; Wu et al., 1994; Xu et al., 1994) have involved pulsed laser excitation to create AT splittings large enough to overcome Doppler broadening and to overcome wavelength limitations imposed by cw lasers. Light shifts in the two-photon excitation spectra of CO and NO were reported by Girard et al. (1983) and Huo et al. (1985), respectively. Quesada et al. (1987) measured AT splitting in H_2. Using a two-color scheme, Xu et al. (1994) measured the AT splitting and AC-Stark shifts in the (2 + 2) resonance-enhanced multiphoton ionization (REMPI) spectrum of CO. The AC-Stark effect in the (2 + 2) REMPI spectrum of N_2 and two-photon laser-induced fluorescence of CO was measured by Girard et al. (1992).

In contrast, it has been demonstrated that cw multiple resonance excitation schemes can be used to enable AT splitting experiments in Doppler broadened systems (Ahmed & Lyyra, 2007) without the parasitic loss of population due to multi-photon ionization as often occurs with pulsed lasers. In these experiments the velocity group selection by the first resonant laser excitation step results in sub-Doppler resolution for the subsequent excitation steps. Therefore, with the correct laser excitation geometry, modest Rabi frequencies in the range of a few hundred MHz are sufficient to overcome both the residual Doppler broadening and the inherent weakness of the molecular transition dipole moment matrix elements.

Consequently, EIT and AT splittings have been investigated experimentally in Doppler-broadened Li_2 (Ahmed et al., 2011; Lazoudis et al., 2010; Qi & Lyyra, 2006; Qi et al., 1999; Qi et al., 2002), K_2 (Li et al., 2005), and Na_2 (Ahmed et al., 2006; Ahmed et al., 2008 Ahmed et al., 2009; Lazoudis et al., 2008; Lazoudis et al., 2011; Yi et al., 2004) gases contained in

heat-pipe ovens, while Cs_2 was studied in a vapor cell (Li et al., 2010). In addition, Benabid and coworkers (Benabid et al., 2005a; Benabid et al., 2005b; Benabid et al., 2005c) have discussed applications of coherence effects for molecules confined in a hollow core fiber, and relevent experiments on acetylene were carried out in a photonic microcell by Light et al. (2009) and in a hollow-core photonic-gap fiber by Ghosh et al. (2005).

1.3 Present Work

The purpose of the present chapter is to describe our recent work on the AT effect in alkali diatomic molecules, including applications involving angular momentum alignment, absolute measurements of transition dipole moment functions, and quantum control of spin–orbit perturbations. We present the important features of molecular AT and its applications.

The AT effect can be used for all-optical control of molecular angular momentum alignment of nonpolar molecules (Qi et al., 1999). The AT splitting is proportional to the Rabi frequency, which in turn depends on the $|M_J|$ values of the transition. Thus levels with different values of $|M_J|$ will become split apart in energy by the AT effect. A weak probe laser can therefore be tuned to resonance with selected M_J levels, in principle leading to complete alignment of the excited molecules.

The AT effect can also used as a precision probe of the molecular electronic transition dipole moment (Ahmed et al., 2006; Qi et al., 2002) and its dependence on internuclear separation (Ahmed et al., 2008; Salihoglu et al., 2008; Sweeney et al., 2008). In this application, an accurate measurement of the coupling laser electric field amplitude and a detailed simulation of the AT split line shape are essential elements. Accurate measurements of the electronic transition dipole moment matrix element, a key parameter in the Einstein A coefficient, are of broad interest. The AT based measurements avoid some of the systematic problems associated with lifetime and calibrated intensity measurements, which traditionally have been used to extract information about the electronic transition dipole moment. Use of lifetime measurements to infer electronic transition moments suffers from the fact that excited molecular rovibronic levels can generally decay to a large number of levels in one or several lower lying electronic states, and the contribution of each channel to the overall lifetime must be determined. Calibrated intensity measurements, in which the intensities of a number of spectral lines of an electronic transition are measured, avoids this complication, but in general only relative transition dipole matrix elements can be obtained. By combining the Autler–Townes splitting based measurements with calibrated intensity measurements, a transition dipole moment, previously determined only as a relative function in arbitrary units, can be placed on an absolute scale (Ahmed et al., 2008; Sweeney

et al., 2008). This combined approach extends to much weaker transitions the range of the Autler–Townes splitting based measurements. A comparison of experimentally determined $1(A)^1\Sigma_u^+ \leftrightarrow 1(X)^1\Sigma_g^+$ transition dipole moment functions, obtained using the AT method, with state-of-the-art *ab initio* calculations indicates very good agreement for Li_2, the lightest molecule with a core (Salihoglu et al., 2008), as well as for Na_2 (Ahmed et al., 2008). This demonstrates that such experiments can provide critical tests for *ab initio* calculations for a variety of systems.

The AT effect also represents a flexible tool to "tune" the mixing coefficients of a pair of energy levels that are weakly mixed by the spin–orbit interaction (Ahmed et al., 2011). This result suggests that AT could be used to enhance the rate of population transfer to otherwise "dark" states, either by increasing the mixing between existing perturbed pairs of levels or by creating mixed levels out of previously unmixed ones. States with naturally mixed character have been used as "windows" or "gateways" for access to energy levels with different character than the ground state (Lyyra et al., 1991; Xie & Field, 1985). Such perturbed levels have also been used as intermediate levels in the transfer of cold alkali molecules formed at long range in the triplet $a^3\Sigma^+$ state to deeply bound levels of the singlet $X^1\Sigma^+$ ground state (Danzl et al., 2008; Danzl et al., 2009; Deiglmayr et al., 2008; Ghosal et al., 2009; Ni et al., 2008; Sage et al., 2005).

Using the theoretical foundation developed in Kirova and Spano (2005), a frequency domain quantum control scheme, demonstrated in Ahmed et al. (2011), allows control of the spin–orbit interaction, i.e., the ability to tune the mixing coefficients of a pair of mixed singlet and triplet rovibronic levels by varying the electric field amplitude of the coupling laser. The application of this quantum state character control to predissociation dynamics is presently under experimental investigation. In this case the idea is to mix more bound state character into a predissociating rovibronic level and control the breaking of the molecular bond.

This chapter is organized as follows. Section 2 presents a detailed theoretical analysis of the Autler–Townes effect based on the density matrix formalism for several common pump/probe/coupling laser schemes. Section 3 describes the basic experimental setup used in these investigations. Finally, Section 4 discusses various applications of the AT effect in molecules. Conclusions are presented in Section 5.

2. THEORETICAL ANALYSIS

2.1 Density Matrix Formalism

Experiments designed to study coherence effects typically are carried out with an ensemble of particles and thus the use of the density matrix

formalism is generally required in the analysis (Scully & Zubairy, 1997; Shore, 1990; Stenholm, 1984). The evolution of the density matrix $\rho(t)$ of a system in time is governed by the equation of motion

$$\frac{\partial \rho}{\partial t} = -\frac{\mathrm{i}}{\hbar}[H, \rho] + \Gamma, \tag{1}$$

where Γ represents the phenomenological relaxation terms accounting for physical processes such as spontaneous decay of levels, collisions, etc. (Stenholm, 1984). They are incorporated into Equation (1) by means of an $n \times n$ relaxation matrix. In general, the elements of the relaxation matrix can be presented in the form

$$\Gamma_{ij}(\rho) = \delta_{ij}\left(-\left(W_i + W_\mathrm{t}\right)\rho_{ij} + \sum_{\substack{k=1 \\ k \neq i}}^{n} \Theta(\varepsilon_k - \varepsilon_i) W_{ki}\rho_{kk}\right) - \left(1 - \delta_{ij}\right)\gamma_{ij}\rho_{ij}, \tag{2}$$

where δ_{ij} is the Kronecker delta and $\Theta(\varepsilon_k - \varepsilon_i)$ is the Heaviside step function. In general, each molecular level can decay to lower lying electronic states of the system through spontaneous emission. W_i is the total radiative decay rate out of level i ($W_i = 1/\tau_i$ where τ_i is the radiative lifetime of state i), W_{ij} is the radiative transition rate from level i to level j, and the γ_{ij} are phenomenological parameters representing the damping rate at which the off-diagonal elements of the density matrix relax toward equilibrium. They are defined by

$$\gamma_{nm} = \frac{1}{2}\sum_k \left(W_{nk} + W_{mk}\right) + \gamma_{nm}^\mathrm{c}, \quad n \neq m, \tag{3}$$

where γ_{nm}^c represents the rate of decay of the nm coherence due to collisions with other atoms or molecules. For levels that cannot decay radiatively, the rate at which the molecules escape the interaction region (beam-transit rate W_t) is the dominant process, which must be taken into account. For the systems and experiments discussed here, $W_\mathrm{t}/2\pi$ is of the order of 1 MHz, calculated according to Sagle et al. (1996). If level i is a thermally populated level of the ground state, then a positive term, proportional to W_t and representing repopulation of level i by fresh molecules entering the beam, must be added to the right-hand side of Equation (2).

Coherent effects are generally only observable when two (or more) coherent light sources (lasers) interact with the same atomic or molecular energy level. The most common excitation schemes used to realize such observations with two lasers are the Cascade, Lambda, and Vee schemes (see Figure 1). Often it is advantageous to have independent control of the

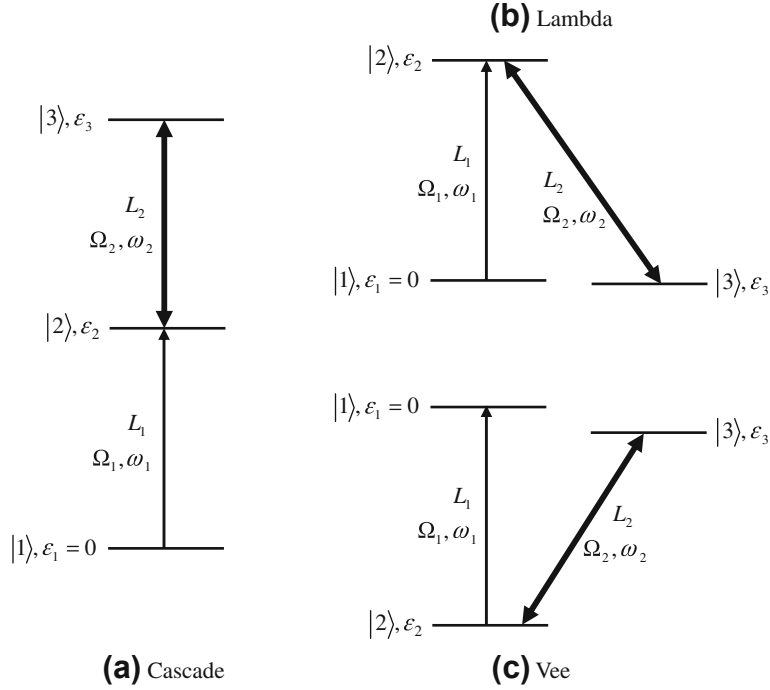

Figure 1 Schematic diagram of coherent excitation processes of three-level, double resonance Cascade (a), Lambda (b), and Vee (c) schemes. In each case, L_2 is taken to be the "coupling" field, and L_1 is the probe field.

coupling transition. This can be realized using the "extended-Λ" scheme shown in Figure 2, where level $|4\rangle$ can be any (not necessarily thermally populated) ground state level chosen to have a particularly large transition dipole matrix element with level $|2\rangle$.

The alkali molecular systems can be considered open in the sense that the energy levels used to create the coherent effect are also coupled to other energy levels outside the excitation scheme. Therefore, the total population of the coherently coupled levels of an open system is strongly not conserved, due to the many extra rovibrational decay pathways for the excited levels, as shown in Figure 3 for a cascade system. This is in contrast to a closed atomic system, in which no other levels beyond those needed to create the coherence effects are typically involved. For example, in order to take this "openness" of the coherently coupled levels into account in the cascade scheme, two auxiliary states denoted by $|4^*\rangle$ and $|5^*\rangle$ are introduced (see Figure 3). These levels represent all other rovibrational levels of the first excited state ($A^1\Sigma_u^+$ for the alkali experiments described below)

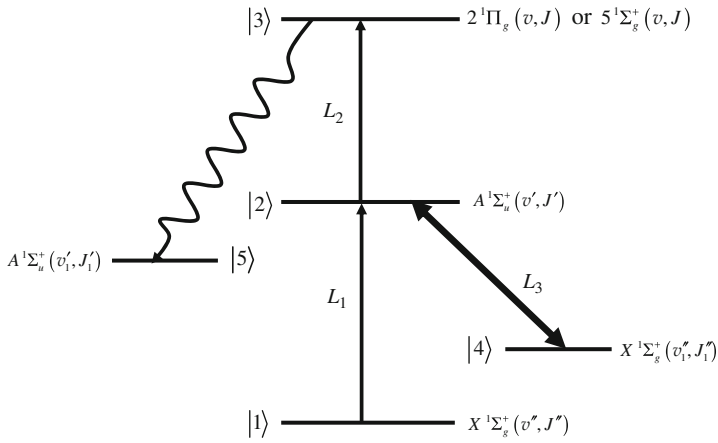

Figure 2 Energy level diagram for the extended-Λ four level system with triple resonance excitation. The pump and probe lasers, L_1 and L_2, are in a co-propagating arrangement and counter-propagate with the coupling field, L_3. For the Na_2 and Li_2 experiments (Ahmed et al., 2008; Salihoglu et al., 2008) $|1\rangle$ denotes the lower level of the L_1 transition, $X^1\Sigma_g^+$ (v'', J''), $|2\rangle$ denotes the intermediate state $A^1\Sigma_u^+$ (v', J'), which is the upper level of the L_1 transition and lower level of the L_2 transition, $|3\rangle$ denotes the upper state level to which the probe laser L_2 is tuned, namely $2^1\Pi_g$ (v, J) or $5^1\Sigma_g^+$ (v, J), and $|4\rangle$ is the lower level $X^1\Sigma_g^+$ (v''_1, J''_1) of the coupling field resonance transition. Level $|5\rangle$ $[A^1\Sigma_u^+$ $(v'_1, J'_1)]$ is the lower level of the $|3\rangle \rightarrow |5\rangle$ fluorescence detection channel used to monitor population in level $|3\rangle$.

and the ground state $(X^1\Sigma_g^+)$ manifolds, respectively, to which decay is allowed.

The total Hamiltonian for the system H can be represented as a sum of two parts:

$$H = H_{\text{mol}} + H_{\text{int}}, \tag{4}$$

where H_{mol} is the Hamiltonian of the unperturbed molecule and H_{int} is the perturbation due to the interaction of the molecule with the external electromagnetic fields. H_{mol} is diagonal in the basis of the unperturbed molecular states and can be expressed as

$$H_{\text{mol}} = \sum_k \varepsilon_k |k\rangle\langle k|, \tag{5}$$

where the ε_k are the energy eigenvalues $(H_{\text{mol}}|k\rangle = \varepsilon_k|k\rangle)$.

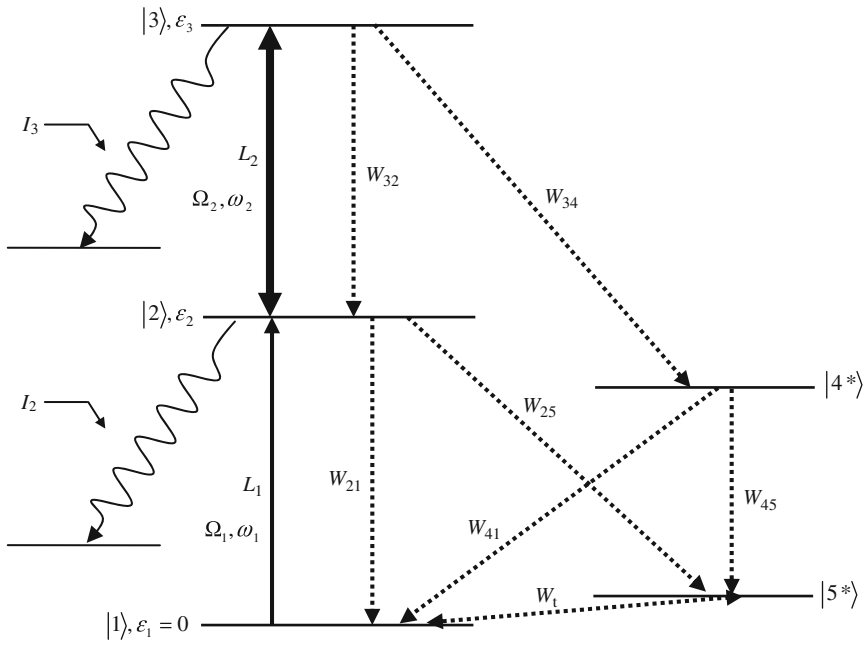

Figure 3 Schematic diagram of excitation and decay processes of the three-level, double resonance cascade scheme. The probe laser L_1 with optical frequency ω_1 and Rabi frequency Ω_1 is tuned through the resonance between levels $|1\rangle$ and $|2\rangle$, while the coupling laser L_2 with optical frequency ω_2 and Rabi frequency Ω_2 is fixed at line center of the $|2\rangle \rightarrow |3\rangle$ resonance. Here I_2 and I_3 represent the intensities of the single channel fluorescence used for detection in experiments with molecules (Ahmed et al., 2006; Ahmed et al., 2011; Qi et al., 1999; Qi et al., 2002). These signals are proportional to the populations of levels $|2\rangle$ and $|3\rangle$, respectively. The dashed arrows indicate possible decay channels from the different energy levels. Due to selection rules, W_{31}, W_{24}, and W_{35} are zero for homonuclear molecules. Levels $|4^*\rangle$ and $|5^*\rangle$ indicate other possible decay channels rendering the system open. The beam-transit relaxation rate W_t is included to account for the rate with which the molecules escape from the interaction region. It is only significant for levels $|1\rangle$ and $|5^*\rangle$ which cannot radiatively decay.

For the analysis of coherence effects, the use of a semiclassical approach where the atoms (molecules) are treated quantum mechanically and the electromagnetic fields are treated classically, is often sufficient. H_{int} includes the interactions between the molecule and the electric fields of the lasers. In the dipole approximation these terms have the form $-\boldsymbol{\mu}\cdot\mathbf{E}$, where $\boldsymbol{\mu}$ is the dipole moment for the transition between the levels coupled by the corresponding laser with electric field $\mathbf{E}$. Further, we assume that the molecules interacting with the electromagnetic radiation experience spatially homogenous electric fields $\mathbf{E}$, as the extent of the molecular electronic wave function is generally much smaller, at thermal temperatures, than the

wavelength λ of electromagnetic radiation in the visible or near infrared regions. We also assume that $\mathbf{E}$ is linearly polarized with magnitude E. Thus for $\mathbf{E}$ we have

$$\mathbf{E}(r = 0, t) = E \cos(\omega t)\hat{z}. \tag{6}$$

The interaction Hamiltonian H_{int} introduces off-diagonal elements into the Hamiltonian matrix. It is given by

$$H_{\text{int}} = \frac{1}{2} \sum_k \hbar\Omega_k \left(|l_k\rangle\langle m_k| + |m_k\rangle\langle l_k| \right) \left(\mathrm{e}^{\mathrm{i}\omega_k t} + \mathrm{e}^{-\mathrm{i}\omega_k t} \right), \tag{7}$$

where the summation is over all external electromagnetic fields (i.e., laser fields L_k) with frequency ω_k, amplitude E_k, and Rabi frequency

$$\Omega_k \equiv \frac{\mu E_k}{\hbar}. \tag{8}$$

Here $|l_k\rangle$ and $|m_k\rangle$ represent the lth and mth states that are coupled by laser L_k. We assume that the frequency ω_k of each field is nearly resonant with only one transition and thus able to couple only one pair of levels $|l_k\rangle$–$|m_k\rangle$.

In solving Equation (1) it is useful to use the interaction picture. We illustrate the procedure for obtaining the explicit form of the Hamiltonian of the system in the interaction picture, H_{I}, using the cascade three-level system shown in Figure 1a. H_{mol} [see Equation (5)] can be written as a sum of two parts $H_{\text{mol}} = H^{\text{o}}_{\text{mol}} + H^{\text{d}}_{\text{mol}}$, with $H^{\text{o}}_{\text{mol}}$ involving only the optical frequencies ω_1 and ω_2 of laser fields L_1 and L_2, respectively,

$$H^{\text{o}}_{\text{mol}} = \hbar\omega_1 |2\rangle\langle 2| + \hbar\left(\omega_1 + \omega_2\right) |3\rangle\langle 3|, \tag{9}$$

and $H^{\text{d}}_{\text{mol}}$ involving only the detunings

$$H^{\text{d}}_{\text{mol}} = -\hbar\Delta_1 |2\rangle\langle 2| - \hbar\left(\Delta_1 + \Delta_2\right) |3\rangle\langle 3|. \tag{10}$$

Here, the detunings, Δ_k, of the laser frequencies from the molecular transition frequencies are defined as

$$\Delta_1 \equiv \omega_1 - \frac{\varepsilon_2 - \varepsilon_1}{\hbar} \quad \text{and} \quad \Delta_2 \equiv \omega_2 - \frac{\varepsilon_3 - \varepsilon_2}{\hbar}. \tag{11}$$

Using the unitary transformation $\rho_{\text{I}} = U^{\dagger}\rho U$, with $U = \exp\left(-\mathrm{i}H^{\text{o}}_{\text{mol}}t/\hbar\right)$, the system can be written in the interaction picture, which transforms Equation (1) into

$$\frac{\partial \rho_{\text{I}}}{\partial t} = -\frac{\mathrm{i}}{\hbar}[H_{\text{I}}, \rho_{\text{I}}] + \text{relaxation terms}. \tag{12}$$

The Hamiltonian of the system in the interaction picture H_{I} has the form:

$$H_{\text{I}} = U^{\dagger}\left(H^{\text{d}}_{\text{mol}} + H_{\text{int}}\right) U. \tag{13}$$

After incorporating the explicit forms of $H_{\text{mol}}^{\text{d}}$ and H_{int} into Equation (13) and applying the rotating wave approximation to eliminate the high frequency oscillating terms, the following explicit form for H_{I} is obtained:

$$H_{\text{I}} = -\hbar\Delta_1|2\rangle\langle 2| - \hbar\left(\Delta_1 + \Delta_2\right)|3\rangle\langle 3| + \frac{\hbar}{2}\Omega_1\left(|1\rangle\langle 2| + |2\rangle\langle 1|\right) + \frac{\hbar}{2}\Omega_2\left(|2\rangle\langle 3| + |3\rangle\langle 2|\right). \tag{14}$$

The Hamiltonian H_{I} for the V (Lazoudis et al., 2011), Λ (Lazoudis et al., 2010), Γ (Qi et al., 1999), extended-Λ (Ahmed et al., 2006), and other schemes can be derived in a similar manner.

By combining the Hamiltonian from Equation (14) with the equation of motion Equation (12) along with all possible decay processes included in $\Gamma(\rho)$ (as shown in Figure 3), the individual components of the density matrix equation of motion can be obtained. Because only cw lasers are involved in the experiments to be discussed in this work, a steady-state approximation can be made in the resulting system of equations, which transforms them from a set of first-order differential equations to a simple set of homogeneous linear equations. This set of linear equations, combined with the equation representing conservation of total population in the system ($\sum_i \rho_{ii} = 1$), can be solved numerically. The population conservation equation transforms the homogeneous system of linear equations obtained using the steady-state approximation in Equation (12) into an inhomogeneous system.

In optical experiments with hot gaseous samples, the Doppler shift in the frequency of the laser radiation due to the motion of the atoms (molecules) has a significant effect and has to be taken into account in the analysis and interpretation of the experimental results. The numerically calculated density matrix elements of Equation (12) are functions of the component of molecular velocity along the laser beam propagation axis. For a particle moving with a velocity v, the shift in the frequency of the laser radiation it "sees" is given by $\omega = \omega_{\text{lab}}\left(1 \pm \frac{\text{v}}{c}\right)$, where the positive sign is for the case of motion towards the source of the radiation and the negative sign is for the case of motion away from the source. ω_{lab} is the lab frame frequency of the laser. Then we define the velocity dependent detuning of the kth laser as $\delta_k \equiv \Delta_k \pm \frac{\omega_{k,\text{lab}}}{c}\text{v}$. Thus the Hamiltonian from Equation (14) for a molecule moving with velocity v becomes:

$$H_{\text{I}} = -\hbar\delta_1|2\rangle\langle 2| - \hbar\left(\delta_1 + \delta_2\right)|3\rangle\langle 3| + \frac{\hbar}{2}\Omega_1\left(|1\rangle\langle 2| + |2\rangle\langle 1|\right) + \frac{\hbar}{2}\Omega_2(|2\rangle\langle 3| + |3\rangle\langle 2|). \tag{15}$$

In thermal equilibrium, the velocity distribution of the particles of a gas is Maxwellian, and averaging of the density matrix over the distribution is

required,

$$\langle \rho_{ij} \rangle_{v_z} = \int_{-\infty}^{\infty} \rho_{ij}(v_z) N(v_z) dv_z. \tag{16}$$

In Equation (16) v_z is the component of particle velocity along the laser propagation direction and $N(v_z)$ is the one dimensional Maxwell distribution given by

$$N(v_z) = \frac{1}{v_p \sqrt{\pi}} \exp\left(-\frac{v_z^2}{v_p^2}\right), \tag{17}$$

where $v_p = (2kT/m)^{1/2}$ is the most probable velocity of a molecule with mass m at temperature T.

Doppler broadening also complicates the observation of the AT splitting. For example, as predicted by Ahmed and Lyyra (2007) and observed by Lazoudis et al. (2008), AT splitting in the fluorescence from level $|3\rangle$ in the cascade excitation scheme depends critically on the wavenumber ratio of the coupling and probe lasers for an inhomogeneously broadened sample.

An additional effect that must be considered is the existence of magnetic sublevels M_J, as each rovibrational level with rotational quantum number J consists of $2J + 1$ sublevels. In the presence of a strong external laser field, the degeneracy of these levels is removed and the transition dipole matrix element is then a function of the magnetic quantum number M_J. The functional dependence is given by the so-called orientation factors introduced by Spano (2001), which depend on the angular momenta of the electronic transition, and the polarization of the electromagnetic radiation. Thus summation (taking selection rules into account) over the magnetic quantum number M_J is required in the calculation of the density matrix elements:

$$\langle \rho_{ij} \rangle_{v_z, M_J} = \sum_{M_J} \int_{-\infty}^{\infty} \rho_{ij}^{M_J}(v_z) N(v_z) dv_z. \tag{18}$$

The final averaging that needs to be performed arises from the radial distribution of the electric field amplitude within the laser beam profile due to its Gaussian spatial distribution,

$$E(r) = E_0 \exp\left(-\frac{r^2}{w^2}\right), \tag{19}$$

where w and E_0 are the laser beam spot size and the electric field amplitude at the center of the beam, respectively. The spatial variation of the electric field causes spatial variation of the Rabi frequency, and as the detection system in each experiment collects photons from the whole interaction region, a radial averaging is required. This need for averaging can be avoided if the strong (coupling) laser beam radius is made to be at least two to three times larger than the probe laser beam radius.

Then the probe beam will "probe" a region in space where the coupling laser intensity is approximately constant.

After calculating the density matrix elements and performing all the required averaging, the calculated population of level $|i\rangle$, represented by $\langle\rho_{ii}\rangle$, can be directly compared to the experimentally measured fluorescence signal from this level (to which it is proportional).

2.2 Dressed State Approach

The semiclassical approach discussed above is a relatively simple and convenient method for simulating the experimental spectra. A more generalized approach for the theoretical analysis of the problem of the interaction of a strong optical field with an atom or molecule is the dressed state formalism (Cohen-Tannoudji et al., 2004; Cohen-Tannoudji & Reynaud, 1977) in which both the atom/molecule and the optical field are treated quantum mechanically. To illustrate the dressed state approach we consider the $|3\rangle \leftarrow |2\rangle$ coupling laser transition of the three-level cascade scheme shown in Figure 1a. In the dressed state approach, the levels are depicted as shown in Figure 4. The Hamiltonian for this system is:

$$H = H_{\text{mol}} + H_{\text{f}} + H_{\text{int}}, \tag{20}$$

[compare Equation (4)] where the new term, H_{f}, is the Hamiltonian of the quantized laser field. The molecular part of the Hamiltonian H_{mol} is given by Equation (5) and H_{int} is given by Equation (7). The Hamiltonian of the optical field H_{f} can be expressed as

$$H_{\text{f}} = \hbar\omega_2 \left(a^{\dagger}a + \frac{1}{2}\right), \tag{21}$$

where $a^{\dagger}$ and a are the photon creation and annihilation operators, and ω_2 is the coupling laser (L_2) frequency. The eigenstates of $H_{\text{mol}} + H_{\text{f}}$ are labeled by the atomic or molecular bare state quantum number $|k\rangle$ and by the number of photons in the field N (see Figure 4). The states $|2, N+1\rangle$ and $|3, N\rangle$ are nearly degenerate with a separation equal to the laser detuning from resonance; $\hbar\delta_2 = \hbar(\omega_2 - \omega_{32})$. Here ω_{32} is the $|3\rangle \leftarrow |2\rangle$ resonance frequency. The relative positions of $|2, N+1\rangle$ and $|3, N\rangle$ depend on the coupling laser detuning δ_2. For $\delta_2 < 0$, $|2, N+1\rangle$ lies below $|3, N\rangle$ and for $\delta_2 > 0$, $|2, N+1\rangle$ lies above $|3, N\rangle$.

The pairs of levels, $|2, N+1\rangle$ and $|3, N\rangle$, for different values of N form a ladder of levels with adjacent pairs separated by the coupling laser photon energy $\hbar\omega_2$. The interaction part of the Hamiltonian, H_{int},

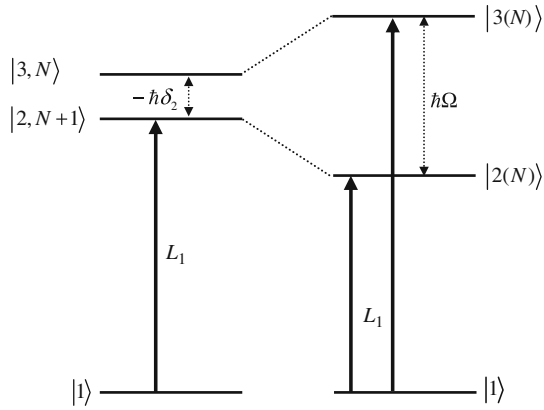

Figure 4 Dressed state diagram demonstrating the AT splitting of the probe laser transition in the three level cascade scheme shown in Figure 1a. The interaction between the molecule and the field of the strong coupling laser L_2 (tuned near resonance with the $|3\rangle \leftarrow |2\rangle$ transition) transforms the uncoupled states (left side of diagram) into the dressed states (right side), as described in the text. When the frequency of the probe laser (L_1) is scanned across the transitions from the lower level $|1\rangle$ to the pair of dressed state levels, a doublet structure is observed. Resonances occur at $\omega_{12} \mp \Omega/2$.

is given by

$$H_{\text{int}} = \frac{\hbar\Omega_2}{2}(|3\rangle\langle 2| + |2\rangle\langle 3|)(a + a^{\dagger}), \tag{22}$$

which couples the two states of each manifold. As a result of this interaction, two new states labeled as $|2(N)\rangle$ and $|3(N)\rangle$ (Cohen-Tannoudji et al., 2004; Weiner & Ho, 2003), separated by $\hbar\Omega = \hbar\sqrt{\delta_2^2 + \Omega_2^2}$, are created. The states $|2(N)\rangle$ and $|3(N)\rangle$ can be represented as superpositions of the uncoupled $|2, N+1\rangle$ and $|3, N\rangle$ states:

$$\begin{aligned} |2(N)\rangle &= \sin\theta|3,N\rangle + \cos\theta|2,N+1\rangle, \\ |3(N)\rangle &= \cos\theta|3,N\rangle - \sin\theta|2,N+1\rangle, \end{aligned} \tag{23}$$

where the angle θ is defined through $\tan\theta = -\Omega_2/\delta_2$.

When the frequency of the weak probe laser L_1 is tuned across the resonances $|1\rangle \rightarrow |2(N)\rangle$ and $|1\rangle \rightarrow |3(N)\rangle$, a doublet structure (the Autler–Townes doublet) is observed.

3. EXPERIMENTAL DETAILS

In the experiments carried out at Temple and Lehigh Universities, the alkali vapors are generated in five-arm stainless steel heat-pipe ovens (Figure 5) with operating temperature of 850 K for lithium and 600–625 K for either sodium or a sodium potassium mixture. Argon gas at a pressure of 100–200 mTorr is used as a buffer gas to confine the metal vapor to the center of the oven. Continuous wave Coherent Autoscan 699-29 and 899-29 dye and titanium sapphire lasers, with 0.5 MHz frequency bandwidth, are used in all experiments to produce the pump, probe, and coupling fields. All laser beams are aligned coaxially, and are linearly polarized in a common direction. The relative direction of propagation of the individual laser beams is chosen so that residual Doppler linewidths are minimized. For example, for the cascade scheme described in Qi et al. (2002), Sweeney et al. (2008), and Lazoudis et al. (2008) (see Figure 1a), the probe and coupling lasers are arranged in a counter-propagating configuration, while in the four-level extended-Λ scheme (Figure 2) the pump and probe laser

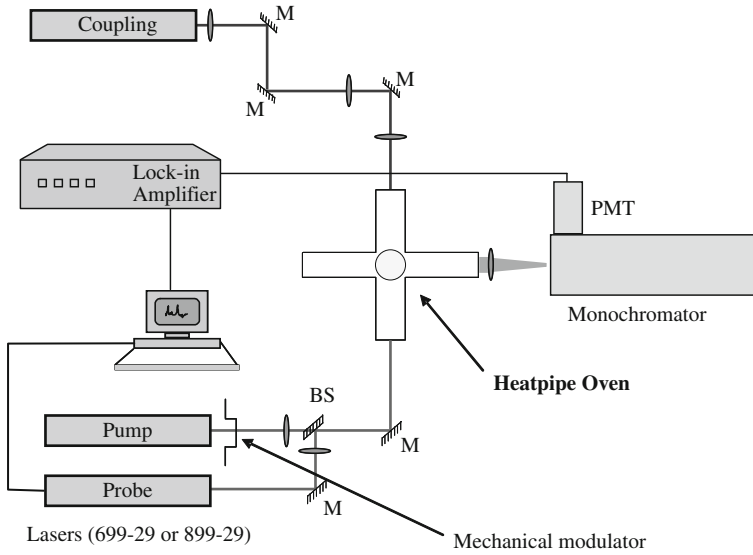

Figure 5 Experimental setup for the four-level (extended-Λ configuration) excitation scheme. The pump and probe lasers co-propagate with each other in the direction opposite to the coupling laser beam direction. A mechanical chopper is used to modulate the pump laser beam, allowing phase-sensitive detection. The resulting double resonance fluorescence signal is detected using a SPEX 1404 double grating monochromator, a photomultiplier tube (PMT), and a lock-in amplifier (SR 850). The signal from the lock-in is recorded by a computer which also controls the laser scan.

beams are generally made to co-propagate, but in the direction opposite to that of the coupling field laser (Ahmed et al., 2006; Ahmed et al., 2008; Salihoglu et al., 2008). The lasers are focused inside the heat pipe to spot sizes of a few hundred micrometers. To ensure relative spatial homogeneity of the coupling electric field amplitude, the spot size of the coupling laser is typically chosen to be at least twice as large as the spot sizes of the probe and pump lasers. It is important to have such an arrangement in order to simplify the theoretical interpretation of the experimental spectra. Tighter focusing of the pump and probe lasers (relative to that of the coupling laser) restricts the observed fluorescence to the spatial region corresponding to the center of the coupling laser electric field amplitude Gaussian radial distribution, and thus the molecules in the overlap region experience a more uniform coupling laser electric field leading to a better resolved AT splitting line profile. The desirable spot size for each laser is obtained with a lens or a combination of two lenses. Neutral density filters are used to control the power of the lasers, and the spot sizes of the laser beams are measured carefully in the interaction region with a razor blade technique (Skinner & Whitcher, 1972) in order to determine the electric field amplitude of each laser. The electric field amplitude, E, for a given laser beam, is related to the measured laser power, P, and the spot size, w, by the expression

$$E = \sqrt{\frac{2}{c\varepsilon_0}}\sqrt{\frac{8P}{\pi w^2}}. \tag{24}$$

Here the spot size, w, is defined as the beam diameter, measured at the $1/e^2$ points of the Gaussian beam intensity profile. We estimate, based on repeated measurements, that the error in a particular laser spot size measurement is about 10 μm, which is also the smallest step size of the micrometer used to drive the razor blade across the beam profile for the beam diameter measurement. The power of the laser beams can be measured with an absolute accuracy of about 1.5%.

A mechanical chopper is used to modulate either the probe or the pump beam so that phase-sensitive detection can be employed. Filtered photomultiplier tubes are used to collect the total fluorescence corresponding to particular molecular bands. In addition, for experiments carried out at Temple University, a SPEX 1404 double grating monochromator is used to detect the molecular fluorescence corresponding to a selected single rovibronic fluorescence transition in a direction perpendicular to the laser propagation direction. The signal from the PMT is fed to a lock-in amplifier (SR 850) with a 300 ms time constant. The probe laser is scanned with a step size of 1 MHz, while the frequencies of all other lasers are fixed to the resonance frequencies of the respective transitions. The individual transitions used in each experiment are identified and verified by

observing resolved fluorescence spectra corresponding to transitions from the excited states to lower lying states.

All laser frequencies are calibrated against lines in the iodine atlas (Gerstenkorn & Luc, 1978, 1979) as a reference. Initially the two or three laser beams are visually overlapped carefully in a direction determined by two iris diaphragms. Then the overlap is further optimized by maximizing the optical–optical double resonance (OODR) fluorescence signal in the case of the three-level system, while for the four-level scheme, various combinations of two laser OODR fluorescence signals are used. For final optimization of the beam overlap, the magnitude of the observed AT splitting is used. Once achieved, the best possible overlap is maintained for the duration of a particular set of experiments.

4. APPLICATIONS TO MOLECULES

4.1 Angular Momentum Alignment of Nonpolar Molecules

The AT splitting induced by a laser is proportional to the Rabi frequency of the corresponding transition. The Rabi frequency, in turn, depends on the molecule's orientation as well as on the amplitude of the electric field of the laser. Thus, one can extend the degree of quantum state selectivity to the degenerate magnetic sublevels by choosing a proper laser excitation scheme, laser polarizations, and laser field strengths (Qi et al., 1999). Control of molecular alignment is one of the most important goals in the study of modern reaction dynamics (Levine & Bernstein, 1974; Linskens et al., 1994; Stolte, 1988). Currently, the DC-Stark shift is the most commonly used technique to create molecular alignment, but it can only be used with polar molecules. An all-optical method has advantages over techniques based on DC fields (Friedrich et al., 1994; Loesch & Remscheid, 1990) because it can also be used to align nonpolar molecules. In the following, the all-optical method introduced in Qi et al. (1999) of attaining molecular alignment in a Doppler broadened diatomic lithium sample will be presented.

For a given rotational quantum number J and for Q type transitions ($\Delta J = 0$), the AT splitting of each individual $|M_J|$ pair of components is equal to the corresponding coupling laser Rabi frequency which is linearly proportional to the $|M_J|$ value; i.e., $\Omega = \frac{|M_J|}{\sqrt{J(J+1)}} E\langle v|\mu_e|v'\rangle/\hbar$. Therefore, as demonstrated in the experiment, the individual $|M_J|$ levels can be separated using the AT splitting. For large J, the separation between the adjacent magnetic levels, after they split, is approximately inversely proportional to J. At the heat-pipe oven temperature of ~1000 K, the Doppler linewidth is about 2.7 GHz. However, the optical–optical double resonance (OODR) excitation allows selection of a single molecular velocity group resulting in

a sub-Doppler linewidth as low as 40 MHz. This is still much larger than the separation between adjacent $|M_J|$ components for a typical 100 W/cm^2 cw laser intensity and typical J values around 18. However, it is possible to resolve the individual $|M_J|$ components for very low rotational quantum numbers.

The selected Li_2 energy levels and the excitation scheme used in the experiment of Qi et al. (1999) are shown in Figure 6a. The pump laser L_1 excites molecules from the ground state level $X^1\Sigma_g^+$ ($v = 2, J = 4$) to a selected intermediate level $A^1\Sigma_u^+$ ($v = 10, J = 3$). The probe laser L_2 further excites the molecule to the upper level $G^1\Pi_g$ ($v = 12, J = 3, f$ parity). The coupling laser L_3 couples the upper level $G^1\Pi_g$ ($v = 12, J = 3, f$) to a second intermediate level $A^1\Sigma_u^+$ ($v = 14, J = 3$) and causes AT splitting in both levels, which is observed by detection of single channel fluorescence from the level $|3\rangle$.

The experimental spectrum in Figure 6b shows that there are three sets of twin peaks due to the AT splitting created by the coupling laser L_3, and which correspond to $|M_J| = 1$, 2, and 3. The slight asymmetry of the peaks is due to an unintentional detuning of the coupling laser of approximately

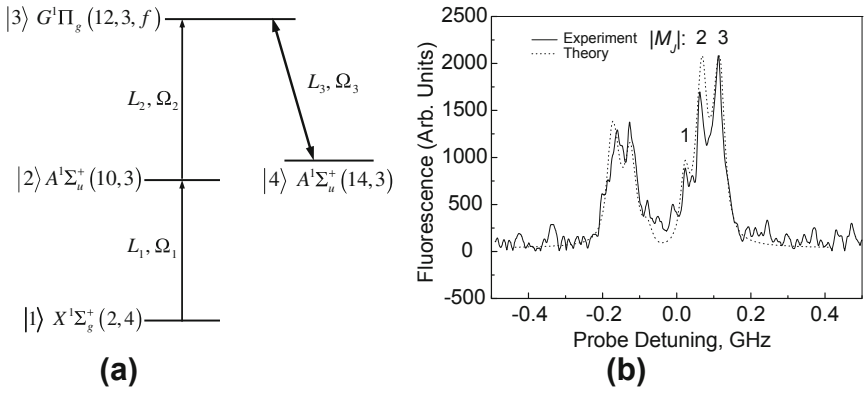

Figure 6 (a) Li_2 energy level diagram and laser excitation scheme used in the angular momentum alignment experiment. (b) Fluorescence detected for a single rovibronic transition (single channel fluorescence) starting in the $G^1\Pi_g$ ($v = 12, J = 3, f$) level, recorded as a function of probe laser (L_2) detuning, displaying the Autler–Townes splitting due to the coupling laser (300 mW) tuned to the $G^1\Pi_g$ ($v = 12, J = 3, f$) $\leftrightarrow$ $A^1\Sigma_u^+$ ($v = 14, J = 3$) transition. The magnetic quantum sub-state dependent Autler–Townes splitting shows that excited Li_2 molecules can be significantly aligned by selective excitation to a specific $|M_J|$ level when the probe laser frequency is tuned to the corresponding AT splitting position with the coupling laser (L_3) on resonance. The solid line is the experimental spectrum while the dotted line represents a theoretical calculation. Figure 6b reprinted with permission from Qi et al. (1999). Copyright 1999 by the American Physical Society.

37 MHz, which is within the uncertainty of the laser wave meter reading. The $|M_J| = 2$ and 3 peaks are fairly well resolved, whereas the $|M_J| = 1$ peak appears to be present, but is just at or below the noise level. The noise here is due to laser intensity fluctuations and frequency drift as well as to the PMT dark current. However, the experiment clearly shows that by tuning the probe laser, the $|M_J|$th magnetic sublevel peak can be selected, thereby preparing aligned excited molecules which predominantly populate the substates $\pm M_J$.

4.2 AT Splitting Measurement of the Transition Dipole Moment

Absolute intensities of molecular rovibronic transitions and their dependence on the electronic transition dipole moment (Herzberg, 1950; Mitchell & Zemansky, 1971) are of fundamental and general interest for many investigations of molecular processes. However, accurate measurements of absolute intensities are notoriously difficult. The situation in molecules is much more complicated than in atomic systems, since in molecules, the electronic transition dipole moment function depends on the internuclear separation.

However, as shown in Qi et al. (2002), Quesada et al. (1987), and Garcia-Fernandez et al. (2005), the AT quantum interference can be used to determine the absolute magnitude of the electronic transition dipole matrix element $\mu_{jk} = \langle v_j, J_j|\mu_e(R)|v_k, J_k\rangle$ for a given transition by determining the Rabi frequency from the measured AT splitting and accurately measuring the coupling laser E field amplitude. The use of a four-level extended-Λ triple resonance excitation scheme for such a measurement was demonstrated for a specific rovibronic transition between the ground and the first excited states by Ahmed et al. (2006). The internuclear distance dependence of the electronic transition dipole moment function, $\mu_e(R)$, for the $A^1\Sigma_u^+$–$X^1\Sigma_g^+$ system was determined for Na_2 by Ahmed et al. (2008) and for Li_2 by Salihoglu et al. (2008). In principle, a simpler two-laser 3-level cascade excitation scheme can be considered for such a study of transition dipole moments between the ground and the excited states. But, as shown by Ahmed et al. (2006), due to saturation broadening, that simpler scheme is less favorable for a Doppler broadened sample with a thermal population distribution in the ground state. The extended-Λ scheme of Figure 2 overcomes this and other difficulties by dedicating separate lasers to the roles of the pump and coupling lasers. Thus a low-power, narrow-band pump laser can be used to select a narrow velocity group from the Doppler broadened transition in order to enhance the resolution of the probe laser scan, whose sole purpose is to reveal the AT splitting of the intermediate level. The coupling laser can be tuned onto resonance with transitions involving levels lying outside the range of thermally populated ground state levels. The ability to choose the coupling laser transition independently of the

pump transition has the additional benefit of allowing measurements of transition dipole moments of a large number of rovibronic transitions between the ground and excited states. These can then be used to construct the $\mu_e(R)$ internuclear distance dependence of the electronic transition dipole moment. Later, Ahmed et al. (2009) have shown how the accessibility of states and transition dipole moments can be further expanded using a five-level quadruple resonance excitation scheme.

Figure 2 illustrates the general energy level diagram of the extended-Λ excitation scheme. In the experiments (Ahmed et al., 2006; Ahmed et al., 2008; Salihoglu et al., 2008) the L_1 pump laser was tuned to resonance on the $A^1\Sigma_u^+\ (v', J') \leftarrow X^1\Sigma_g^+\ (v'', J'')$ transition with the lower level selected from among the thermally populated levels. In order to select a narrow velocity component within the Doppler profile, the L_1 power was kept as low as possible while maintaining a reasonable signal-to-noise ratio in the AT split spectra. The AT splitting of level $|2\rangle$ $[A^1\Sigma_u^+\ (v', J')]$, caused by the strong coupling laser L_3 on resonance with the transition $|2\rangle \leftrightarrow |4\rangle$ $[A^1\Sigma_u^+\ (v', J') \leftrightarrow X^1\Sigma_g^+\ (v_1'', J_1'')]$, was then detected in the fluorescence spectrum originating from upper level $|3\rangle$ as the weak L_2 probe laser was scanned over the $|3\rangle \leftarrow |2\rangle$ transition [either $2^1\Pi_g\ (v, J) \leftarrow A^1\Sigma_u^+\ (v', J')$ or $5^1\Sigma_g^+\ (v, J) \leftarrow A^1\Sigma_u^+\ (v', J')$]. Fluorescence corresponding to an isolated rovibronic transition $|3\rangle \rightarrow |5\rangle$ [single channel $2^1\Pi_g\ (v, J) \rightarrow A^1\Sigma_u^+\ (v_1', J_1')$ or $5^1\Sigma_g^+\ (v, J) \rightarrow A^1\Sigma_u^+\ (v_1', J_1')$ fluorescence], was used to monitor the population of the upper state $|3\rangle$. In all cases, for level $|4\rangle$ the authors have chosen a rotational level belonging to a high vibrational level of the ground state, which lies outside the range of the thermally populated levels.

Simulations of the experimentally recorded AT split spectra were performed using the density matrix formalism outlined in Section 2 above. The Rabi frequency of the coupling field, Ω_3, was varied in the simulations until the best fit to each recorded experimental spectrum was obtained.

The resulting Ω_3 value, along with the strength of the coupling laser electric field, E_3, was then used to calculate the transition dipole moment matrix element between the rovibrational levels coupled by L_3. Equation (24) was used to calculate the coupling laser electric field strength. From the definition of the L_3 coupling laser Rabi frequency, $\Omega_3 = \mu_{24}E_3/\hbar$, the transition dipole matrix element μ_{24} for the coupling transition was then determined. For the experiments quoted above, the uncertainty in the value of μ_{24} was estimated to be approximately ± 0.2 Debye, arising mainly from the error in the measurement of the spot sizes (± 10 μm), the laser power fluctuation (1–2%), the absolute power calibration of the power meter, and the inherent noise in the recorded spectra.

The transition dipole matrix element represents an overlap integral of the rovibronic wave functions of the two levels, weighted with the electronic transition dipole moment, $\mu_e(R)$; i.e., $\mu_{jk} = \langle v_j', J_j'|\mu_e(R)|v_k'', J_k''\rangle$.

In general the electronic transition dipole moment function, $\mu_e(R)$, for a transition between two electronic states of a diatomic molecule, is a function of the internuclear distance, R, and in many cases this dependence can be quite strong. In some cases *ab initio* calculations are available for $\mu_e(R)$. But in most cases no information at all is available for the functional form of $\mu_e(R)$. Given this situation, it is common to assume that $\mu_e(R)$ is constant, or varies weakly as a function of R. Then the transition dipole moment integral reduces to a simple vibrational overlap integral, $\langle v'_j, J'_j \mid v''_k, J''_k \rangle$, times a constant of proportionality. The square of this vibrational overlap integral is the well-known Franck–Condon factor. The Franck–Condon factor is widely used for estimating relative transition strengths, but is only reliable when $\mu_e(R)$ does not change significantly in the R range of the transitions under consideration. However, if $\mu_e(R)$ strongly depends on R then one has to use the full $\langle v'_j, J'_j | \mu_e(R) | v''_k, J''_k \rangle$ matrix element.

Using either the simple R-centroid approximation, or a more complete polynomial expression that includes higher order R-centroids (Fraser, 1954; Lefebvre-Brion & Field, 2004; Noda & Zare, 1982; Tellinghuisen, 1984; Tellinghuisen, 1985), the internuclear distance dependence of $\mu_e(R)$ can be obtained from the set of experimentally determined transition dipole matrix elements. If we represent $\mu_e(R)$ by a power series in the internuclear distance R,

$$\mu_e(R) = \sum_{i=0}^{\infty} \mu_i R^i, \tag{25}$$

the transition dipole matrix element can be written as

$$\langle v' | \mu_e(R) | v'' \rangle = \langle v' | v'' \rangle \sum_{i=0}^{\infty} \mu_i \overline{R^i}, \tag{26}$$

where $\langle v' | v'' \rangle$ is the vibrational overlap integral, and $\overline{R^i}$ is the ith R-centroid defined as

$$\overline{R^i} = \frac{\langle v' | R^i | v'' \rangle}{\langle v' | v'' \rangle}. \tag{27}$$

If we limit ourselves to the lowest order in Equation (25), the approximation introduced by Condon (1928) is obtained with the matrix element proportional to the vibrational overlap integral, equivalent to the square root of the Franck–Condon factor.

The R-centroid approximation (Fraser, 1954; Lefebvre-Brion & Field, 2004; Noda & Zare, 1982; Tellinghuisen, 1984, 1985) assumes

$$\langle v' | \mu_e(R) | v'' \rangle \approx \langle v' | v'' \rangle \mu_e(\overline{R}), \tag{28}$$

so that the matrix element is approximated by the product of μ_e at the R-centroid value $\overline{R}$ and the overlap integral $\langle v' | v'' \rangle$. By expanding $\mu_e(\overline{R})$ in

a power series in $\overline{R}$, and approximating $\overline{R}^i$ with $\overline{R^i}$, Equation (28) becomes equivalent to Equation (26). The R-centroid approximation becomes exact if $\mu_e(R)$ is a linear function of R.

The first-order R-centroid method is adequate if the vibrational overlap integral is dominated by a relatively small region of R. Such a case is shown in Figure 7a, where the calculated R-centroid value of 3.82 Å corresponds closely to the center of the interval 3.5–4.2 Å where the majority of the overlap integral accumulates. On the other hand, in cases where the integral accumulates over a large interval of R, such as the case shown in Figure 7b, this method is unreliable. In such cases, Equation (26) must be used to fit the experimentally obtained set of transition dipole matrix elements. Usually, truncation at the quadratic or cubic terms in the expansion is sufficient to represent the experimental data. In Ahmed et al. (2008) the experimental data were fitted using a polynomial expansion of the Na_2 $A^1\Sigma_u^+$–$X^1\Sigma_g^+$ electronic transition dipole moment function up to second order in R,

$$\mu_e(R) = \mu_0 + \mu_1 R + \mu_2 R^2, \tag{29}$$

and the values $\mu_0 = -4.2502$ D, $\mu_1 = 6.1046$ D $\cdot$ Å^{-1}, and $\mu_2 = -0.64758$ D.Å^{-2} were obtained for the expansion coefficients. The range in R over which this fitted transition dipole moment is valid can be obtained from the range of the individual transition overlap integrals. $\mu_e(R)$ from

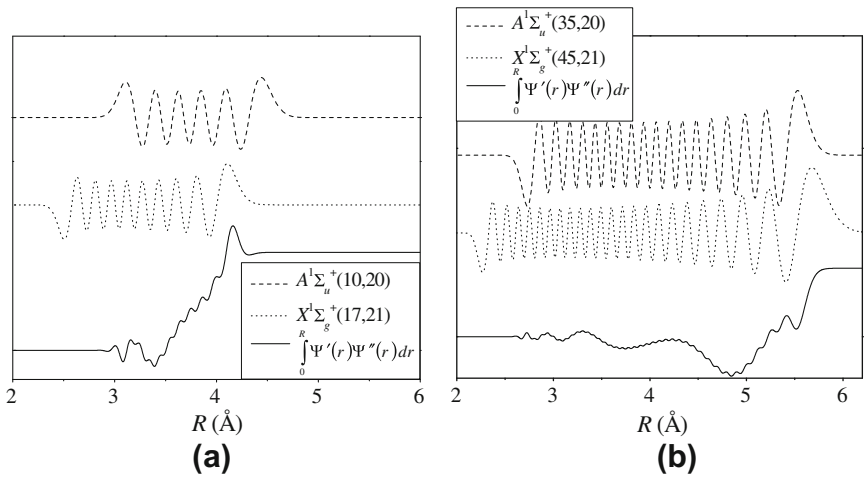

Figure 7 Plots of the Na_2 excited $A^1\Sigma_u^+$ (v', J') and ground $X^1\Sigma_g^+$ (v'', J'') state wave functions Ψ' and Ψ'' and of the overlap integral $\int_0^R \Psi'(r)\Psi''(r)dr$ as functions of the internuclear distance R; (a) for the $A^1\Sigma_u^+$ (10, 20)–$X^1\Sigma_g^+$ (17, 21) transition, and (b) for the $A^1\Sigma_u^+$ (35, 20)–$X^1\Sigma_g^+$ (45, 21) transition. Figure reprinted with permission from Ahmed et al. (2008). Copyright 2008 by the American Physical Society.

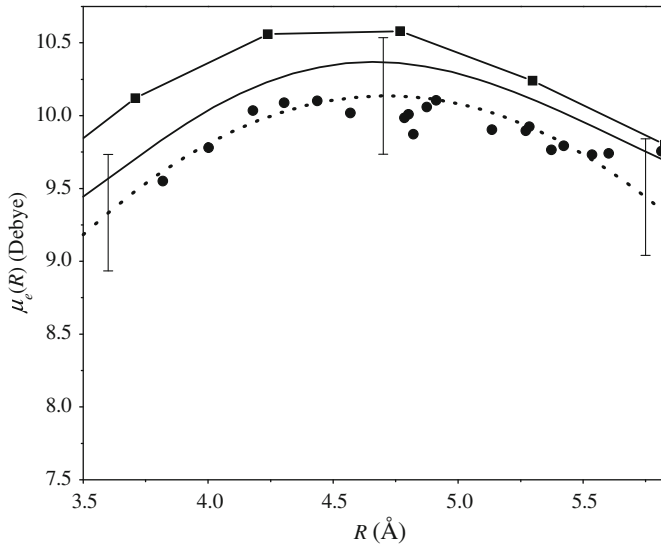

Figure 8 Comparison between the transition dipole moment functions $\mu_e(R)$ obtained from experimental data and pseudopotential (solid line with squares) and relativistic (solid line) *ab initio* calculations for the Na_2 $A^1\Sigma_u^+$–$X^1\Sigma_g^+$ transition. Experimental results from the R-centroid method are given as solid circular dots, while the results from the fit with a quadratic polynomial expansion $\mu_e(R) = \mu_0 + \mu_1 R + \mu_2 R^2$, with coefficients $\mu_0 = -4.2502$ D, $\mu_1 = 6.1046$ D.Å^{-1}, and $\mu_2 = -0.64758$ D.Å^{-2}, are shown as a dotted line. Figure reprinted with permission from Ahmed et al. (2008). Copyright 2008 by the American Physical Society.

Equation (29) is illustrated in Figure 8 (dotted line), while the results from the R-centroid approximation are represented by solid circles. For comparison, results from *ab initio* calculations of the electronic transition dipole moment, $\mu_e(R)$, for the Na_2 $A^1\Sigma_u^+$–$X^1\Sigma_g^+$ system are also shown (Ahmed et al., 2006).

4.3 Combining AT Measurements with Resolved Fluorescence to Map $\mu_e(R)$

After correcting for detection system efficiencies, the relative intensities of resolved fluorescence from a single rovibrational level of one electronic state to the various rovibrational levels of another electronic state can be fit to yield the relative electronic transition dipole moment function $\mu_e(R)$. Such results have been used to test theoretical calculations (Magnier et al., 2000; Ratcliff et al., 1985), albeit only in terms of the *relative* dependence of $\mu_e(R)$ on R. However, as demonstrated in Ahmed et al. (2008), Salihoglu et al. (2008), and Sweeney et al. (2008) and

discussed in this subsection, the range of $\mu_e(R)$ can, in some cases, be extended dramatically by using AT splitting measurements to calibrate relative fluorescence intensity measurements. As discussed above, measurement of the AT splitting allows the determination of the absolute transition dipole matrix element between two levels. Thus AT measurements of a few selected transitions can be used to put the relative transition dipole moment function, $\mu_e(R)$, determined from relative fluorescence intensities, on an absolute scale.

This technique has been described in detail by Sweeney et al. (2008). Those authors used AT splittings, obtained with a three-level pump/probe scheme as shown in Figure 1a, to determine the absolute transition dipole matrix elements between specific levels of the $3^1\Pi$ and $2(A)^1\Sigma^+$ electronic states of the NaK molecule. These results were used to place the relative $3^1\Pi \rightarrow 2(A)^1\Sigma^+$ and $3^1\Pi \rightarrow 1(X)^1\Sigma^+$ transition dipole moment functions, obtained from calibrated fluorescence, onto an absolute scale. For the considered molecular transitions, the transition dipole moment functions vary rapidly with internuclear separation. In addition, the dipole matrix elements are not large, even in the most favorable cases. Thus only a few transition matrix elements can be measured with the AT splitting method. However, the combination of AT splitting with calibrated fluorescence allows a complete mapping of the transition dipole moment functions over fairly broad ranges of R.

The basic experimental setup is similar to that shown in Figure 5. In this case, the heat-pipe oven contained a mixture of sodium and potassium so that NaK molecules were produced in the vapor. A single-mode Ti:Sapphire laser (L_1 in Figure 1a) was used to excite a specific NaK $A^1\Sigma^+(v', J' = 11, e) \leftarrow X^1\Sigma^+(v'', J'' = J' \pm 1, e)$ transition. A single-mode ring dye laser (L_2) was tuned to the $3^1\Pi(v = 19, J = 11, f) \leftarrow A^1\Sigma^+(v', J' = 11, e)$ transition.

A monochromator/PMT combination resolved $3^1\Pi\ (19, 11, f) \rightarrow X^1\Sigma^+\ (v'', 11, e)$ and $3^1\Pi\ (19, 11, f) \rightarrow A^1\Sigma^+\ (v', 11, e)$ fluorescence (see Figure 9a). Lasers L_1 and L_2 were chopped at different frequencies f_1 and f_2 using a dual frequency chopper and signals were processed by a digital lock-in amplifier locked to the sum frequency $f_1 + f_2$. This was necessary in order to distinguish the $3^1\Pi\ (19, 11, f) \rightarrow A^1\Sigma^+\ (v', 11, e)$ fluorescence from the single-laser (L_1 or L_2) induced background light in the same frequency range. Recorded signals from a free-standing violet filtered PMT [which detected the total unresolved $3^1\Pi\ (19, 11, f) \rightarrow X^1\Sigma^+\ (v'', 11, e)$ fluorescence] were used to correct relative resolved peak intensities for small frequency and power fluctuations associated with either laser during the monochromator scans. In addition, light from a calibrated tungsten–halogen white light source (Stair et al., 1963) was sent through the heat pipe and into the monochromator, allowing the relative wavelength-dependent response of the detection system to be determined.

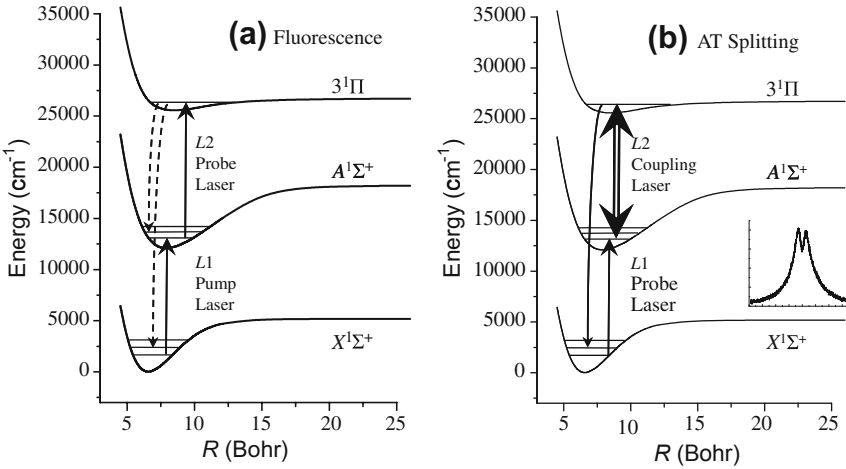

Figure 9 (a) Pumping scheme for measuring resolved $3^1\Pi\ (19, 11, f) \rightarrow A^1\Sigma^+\ (v', 11, e)$ and $3^1\Pi\ (19, 11, f) \rightarrow X^1\Sigma^+\ (v'', 11, e)$ fluorescence transitions. In the notation of Figure 1a, level $|1\rangle$ is $X^1\Sigma^+\ (v'', J' \pm 1, e)$, level $|2\rangle$ is $A^1\Sigma^+\ (v' = 9$ or $10, J' = 11, e)$, and level $|3\rangle$ is $3^1\Pi\ (19, 11, f)$. (b) Pumping scheme for probing the AT splitting lineshape. Total $3^1\Pi \rightarrow X^1\Sigma^+$ fluorescence is detected with a free-standing PMT with short-pass filters. Inset shows an actual AT splitting scan. Figure reprinted with permission from Sweeney et al. (2008). Copyright 2008 by the American Institute of Physics.

The polarization dependence of the detection system (for light linearly polarized either parallel to or perpendicular to the grating grooves) was also determined using a linear polarizer at the monochromator entrance slit. The polarization of the resolved lines was also measured with the same linear polarizer. These results were used to correct the measured fluorescence line intensities. Finally, white light scans recorded when the oven was hot allowed the fluorescence line intensities to be corrected for attenuation due to the relatively small (except at the potassium resonance lines) absorption of fluorescence photons by the alkali vapor in the fluorescence arms of the heat pipe.

Essentially the same experimental setup was used for the AT measurements except that lenses focused the probe and coupling laser beam radii to 120–135 μm and 330–345 μm, respectively. The L_1 probe laser power was reduced to <1 mW in order to minimize power broadening. The L_2 coupling laser power was in the range 240–430 mW to maximize the splitting of the fluorescence lines due to the Autler–Townes effect. With the coupling laser fixed to the $3^1\Pi\ (19, 11, f) \leftarrow A^1\Sigma^+\ (v', 11, e)$ transition, the probe laser was scanned over the $A^1\Sigma^+\ (v', J' = 11, e) \leftarrow X^1\Sigma^+\ (v'', J' \pm 1, e)$ transition, and the total violet fluorescence was recorded, as shown in Figure 9b.

The probe laser frequency dependence of this signal maps out the Autler–Townes lineshape (see Qi et al., 2002).

The $3^1\Pi\ (19, 11, f) \rightarrow X^1\Sigma^+\ (v'', 11, e)$ fluorescence recorded by Sweeney et al. (2008), which occurs in the violet part of the spectrum, was quite clean and was recorded with excellent signal-to-noise even for the weak lines. In contrast, the red $3^1\Pi\ (19, 11, f) \rightarrow A^1\Sigma^+\ (v', 11, e)$ fluorescence was observed in a very congested part of the spectrum, where both lasers pump a number of $A^1\Sigma^+ \leftarrow X^1\Sigma^+$ transitions of NaK and K_2 leading to strong $A^1\Sigma^+ \rightarrow X^1\Sigma^+$ fluorescence bands in addition to the NaK $3^1\Pi \rightarrow A^1\Sigma^+$ fluorescence of interest. Even with modulation of both lasers and lock-in detection at the sum frequency f_1+f_2, the spectrum was still quite congested and noisy. However, the $3^1\Pi\ (19, 11, f)$ level could be pumped using different pump/probe excitation paths, and in each case it was possible to pick out several NaK $3^1\Pi \rightarrow A^1\Sigma^+$ fluorescence lines since they are separated by the known $A^1\Sigma^+$ state vibrational and rotational intervals and since extraneous lines will not appear in all of the spectra obtained with different excitation schemes. Despite the relatively high noise level, background lines, and complete absorption near the strong potassium atomic lines, relative intensities of 11 different $3^1\Pi\ (19, 11, f) \rightarrow A^1\Sigma^+\ (v', 11, e)$ transitions, including the $3^1\Pi\ (19, 11, f) \rightarrow A^1\Sigma^+\ (10, 11, e)$ and $3^1\Pi\ (19, 11, f) \rightarrow A^1\Sigma^+\ (9, 11, e)$ transitions that serve as the absolute AT splitting calibration lines, were successfully recorded. With the white light measurements of the relative detection system efficiency versus wavelength, all of the $3^1\Pi\ (19, 11, f) \rightarrow A^1\Sigma^+\ (v', 11, e)$ and $3^1\Pi\ (19, 11, f) \rightarrow X^1\Sigma^+\ (v'', 11, e)$ fluorescence line intensities could be put on the same relative intensity scale.

Theoretically, since all observed fluorescence transitions are $^1\Pi \rightarrow {}^1\Sigma^+$ Q lines, the relative intensities of the peaks in the resolved NaK $3^1\Pi\,(19, 11, f) \rightarrow A^1\Sigma^+\,(v', 11, e)$ and $3^1\Pi\,(19, 11, f) \rightarrow X^1\Sigma^+\,(v'', 11, e)$ fluorescence scans are given by (Herzberg, 1950)

$$I_{\text{fluorescence}} \propto \nu_{jk}^4 |\mu_{jk}|^2, \tag{30}$$

where j and k represent the upper and lower levels of the transition, respectively, and the transition dipole matrix element $\mu_{jk} = \langle v_j | \mu_e(R) | v_k \rangle$. For the electronic transition dipole moment function $\mu_e(R)$, a polynomial of the form:

$$\mu_e(R) = a_0 + a_1 \left(\frac{R_{eq}}{R}\right)^2 + a_2 \left(\frac{R_{eq}}{R}\right)^4 + \cdots \tag{31}$$

with fitting parameters $a_0, a_1, a_2, \ldots$ was used to fit the calculated intensities to the experimental intensities. Here, $R_{eq} = 4.4587$ Å is the equilibrium internuclear separation of the $3^1\Pi$ state. The computer program LEVEL 8.0 (Le Roy, 2007) was used to calculate the matrix elements of the terms $(R_{eq}/R)^n$ for the measured transitions between the $3^1\Pi\ (19, 11, f)$ level and

the various $A^1\Sigma^+$ $(v', 11, e)$ and $X^1\Sigma^+$ $(v'', 11, e)$ levels. In these calculations, the experimental potentials of Laub et al. (1999), Ross et al. (1988), and Russier-Antoine et al. (2000) were used for the $3^1\Pi$, $A^1\Sigma^+$, and $X^1\Sigma^+$ states, respectively.

A non-linear least squares fit of calculated intensities to the experimentally measured intensities from the resolved fluorescence spectra was carried out to determine the best values for the constants a_i for the $3^1\Pi \rightarrow A^1\Sigma^+$ and $3^1\Pi \rightarrow X^1\Sigma^+$ transition dipole moment functions. The number of fitting parameters was varied, and the best fit was taken to be the one with the lowest reduced chi-squared. The best fit of the $3^1\Pi$ $(19, 11, f) \rightarrow A^1\Sigma^+$ $(v', 11, e)$ spectra included two terms (a_0 and a_1), while four terms ($a_1, a_2, a_3,$ and a_4) yielded the best fit to the $3^1\Pi$ $(19, 11, f) \rightarrow X^1\Sigma^+$ $(v'', 11, e)$ spectra. The a_0 term was excluded from the $3^1\Pi \rightarrow X^1\Sigma^+$ transition dipole moment function since this function is expected to go to zero at large R. This is due to the fact that while the molecular transition is allowed, the atomic transition Na (3S) + K (3D) → Na (3S) + K (4S) is dipole forbidden (as $R \rightarrow \infty$). Note that this fitting of relative intensities provided only relative transition dipole moment functions.

The AT lineshapes were analyzed as described in Sections 2 and 4.2. In this case, the frequency of the strong coupling laser L_2 was fixed to line center of the $3^1\Pi$ $(19, 11, f) \leftarrow A^1\Sigma^+$ $(v', 11, e)$ transition, and the strength of the coupling is described by the Rabi frequency

$$\Omega_2 = \mu_{23}E_2/\hbar = \left\langle 2 \left| \mu_e^{3^1\Pi \rightarrow A^1\Sigma^+}(R) \right| 3 \right\rangle E_2/\hbar, \tag{32}$$

where E_2 is the electric field of the coupling laser. The weak probe laser L_1 was scanned over the $A^1\Sigma^+$ $(v', J' = 11, e) \leftarrow X^1\Sigma^+$ $(v'', J' \pm 1, e)$ transition (see Figure 9b), and the total violet $3^1\Pi$ $(v = 19, J = 11, f) \rightarrow X^1\Sigma^+$ fluorescence, as a function of probe laser frequency, mapped out the AT splitting of the $A^1\Sigma^+$ $(v', J' = 11, e)$ level induced by the coupling laser. Since the violet fluorescence signal is proportional to the population of the $3^1\Pi$ $(19, 11, f)$ level (i.e., ρ_{33} in the notation of Figure 1a) a computer code was used to solve the density matrix equations of motion. The user inputs the measured electric fields and beam radii of the lasers L_1 and L_2, the Rabi frequencies Ω_1 and Ω_2, and the collisional dephasing rates γ_{12}^c, γ_{13}^c, and γ_{23}^c. For known electric field strengths, Γ_{21} and Γ_{32} are not independent of Ω_1 and Ω_2 since both only depend on the dipole matrix elements. The calculations are not very sensitive to the various other radiative rates, which are all known fairly well from theory. The transit relaxation rate W_t was calculated using Equation (8) in Sagle et al. (1996). In the experiment, the probe laser frequency was scanned. Therefore, the program loops over the Maxwell–Boltzmann distribution of velocities, v_z, calculates ρ_{33}^{MM} for each value of $M = M_J$, and reports $\rho_{33} = \sum_M \rho_{33}^{MM}$ for each detuning of the probe laser L_1. Since the exper-

iment uses linearly polarized lasers, the Spano approximation (Spano, 2001) $\sum_{\alpha=-1}^{1}\Gamma_{i(M+\alpha),jM}\rho_{ii}^{M+\alpha,M+\alpha} \approx \rho_{ii}^{MM}\sum_{\alpha=-1}^{1}\Gamma_{i(M+\alpha),jM} = \rho_{ii}^{MM}\Gamma_{ij}$, is employed to simplify the calculations (i.e., this approximation decouples the equations for different values of M). The output is the predicted Autler–Townes lineshape.

The predicted A–T lineshape displays two peaks, in agreement with experiment. The splitting between the peaks is mostly determined by the Rabi frequency Ω_2 of the coupling laser L_2, which causes levels $|2\rangle$ $[A^1\Sigma^+\ (v', J' = 11, e)]$ and $|3\rangle$ $[3^1\Pi\ (19, 11, f)]$ (see Figures 1a and 9b) to each split into two levels (Autler–Townes splitting). Ideally, the probe laser L_1 should be sufficiently weak that the lineshape is independent of Ω_1. However, signal-to-noise concerns required use of L_1 laser intensities such that the fitting was not entirely independent of Ω_1. Ω_1 was calculated from the weighted average of the L_1 electric field over the interaction region and the transition dipole matrix element obtained from LEVEL (Le Roy, 2007) using the theoretical transition dipole moment function of Magnier et al. (2000). The collisional dephasing (line-broadening) rates γ_{12}^{c}, γ_{13}^{c}, and γ_{23}^{c} were found to strongly affect the widths of the peaks and the line wings, but to have relatively little effect on the splitting. Thus Ω_2 was varied until the splitting of the calculated lineshape agreed with experiment, and then the collisional dephasing rates were adjusted to improve the agreement with the overall lineshape. The transition dipole matrix element for the $|2\rangle \leftrightarrow |3\rangle$ transition was then obtained from the measured electric field (weighted average over the interaction region = 0.94 of the peak field) and the fitted Rabi frequency of the coupling laser using Equation (32). From the best fit Rabi frequencies for the $3^1\Pi\ (19, 11, f) \leftarrow A^1\Sigma^+\ (10, 11, e)$ and $3^1\Pi\ (19, 11, f) \leftarrow A^1\Sigma^+\ (9, 11, e)$ transitions, the values $\mu_{3^1\Pi(19,11,f)\leftarrow A^1\Sigma^+(10,11,e)} = (1.51 \pm 0.15)$ Debye and $\mu_{3^1\Pi(19,11,f)\leftarrow A^1\Sigma^+(9,11,e)} = (0.90 \pm 0.09)$ Debye were obtained.

Finally, the program LEVEL 8.0 (Le Roy, 2007) was used to calculate the transition dipole matrix elements $\mu_{3^1\Pi(19,11,f)\leftarrow A^1\Sigma^+(10,11,e)}$ and $\mu_{3^1\Pi(19,11,f)\leftarrow A^1\Sigma^+(9,11,e)}$ from the relative electronic transition dipole moment function $\mu_{e,relative}^{3^1\Pi\rightarrow A^1\Sigma^+}$ obtained from resolved fluorescence. Comparison of these results with the absolute transition dipole matrix elements from the AT splitting experiment then yielded two independent normalization factors that agreed to within 4%. Using the average of the two values, the following expressions for the *absolute* transition dipole moment functions were obtained:

$$\mu_{e,absolute}^{3^1\Pi\rightarrow A^1\Sigma^+}(R) = 11.05 - 5.55\left(\frac{R_{eq}}{R}\right)^2 \tag{33}$$

and

$$\mu_{\mathrm{e,absolute}}^{3^1\Pi\rightarrow X^1\Sigma^+}(R) = 3.40\left(\frac{R_{\mathrm{eq}}}{R}\right)^2 - 11.04\left(\frac{R_{\mathrm{eq}}}{R}\right)^4 + 12.26\left(\frac{R_{\mathrm{eq}}}{R}\right)^6 - 3.88\left(\frac{R_{\mathrm{eq}}}{R}\right)^8, \quad (34)$$

where the transition dipole moments are given in Debye. The absolute magnitudes of these functions are believed to be accurate to ∼15–25%, based on a 5% uncertainty in the determination of the electric field, a 10% uncertainty in determination of the Rabi frequency from the AT splitting lineshapes, and a 10–15% uncertainty in the relative line intensities, especially in the $3^1\Pi \rightarrow A^1\Sigma^+$ fluorescence band, which necessarily had to serve as the calibration point in this experiment. The relative R dependences of these functions are probably accurate to ∼5–10% within each band.

A comparison of experimental and calculated relative fluorescence intensities [using Equations (33) and (34)] is shown in Figure 10. The best-fit transition dipole moment functions $\mu_{\mathrm{e,absolute}}^{3^1\Pi\rightarrow A^1\Sigma^+}(R)$ and $\mu_{\mathrm{e,absolute}}^{3^1\Pi\rightarrow X^1\Sigma^+}(R)$ are plotted in Figure 11a and b, respectively, where they are compared to the recent theoretical calculations of Magnier et al. (2000) and the much earlier calculations of Ratcliff et al. (1985). Figure 11b also shows the relative $3^1\Pi \rightarrow X^1\Sigma^+$ transition dipole moment function obtained by Laub et al. (1999) using calibrated fluorescence alone. It can be seen that the most recent theoretical calculations of Magnier et al. (2000) are in excellent agreement with the experimental results, with regard to both the absolute magnitude and the functional dependence of the transition dipole moment functions.

The above results demonstrate that a combination of resolved fluorescence scans and AT splitting measurements can be used to determine molecular transition dipole moment functions over broad ranges of internuclear separation R. The particular value of combining the two techniques was demonstrated in the Sweeney et al. (2008) experiment where the transition dipole matrix elements were small and the electronic transition dipole moment function strongly dependent on R. In this case, the AT splitting method could only be used to determine the absolute transition dipole matrix elements for a few of the strongest transitions, whereas the resolved fluorescence technique allowed determination of many transition dipole matrix elements, including those for much weaker transitions, but only on a relative scale. The combination of the two techniques allowed all matrix elements to be measured absolutely. Consequently the theoretical transition dipole moment functions can be tested on an absolute basis.

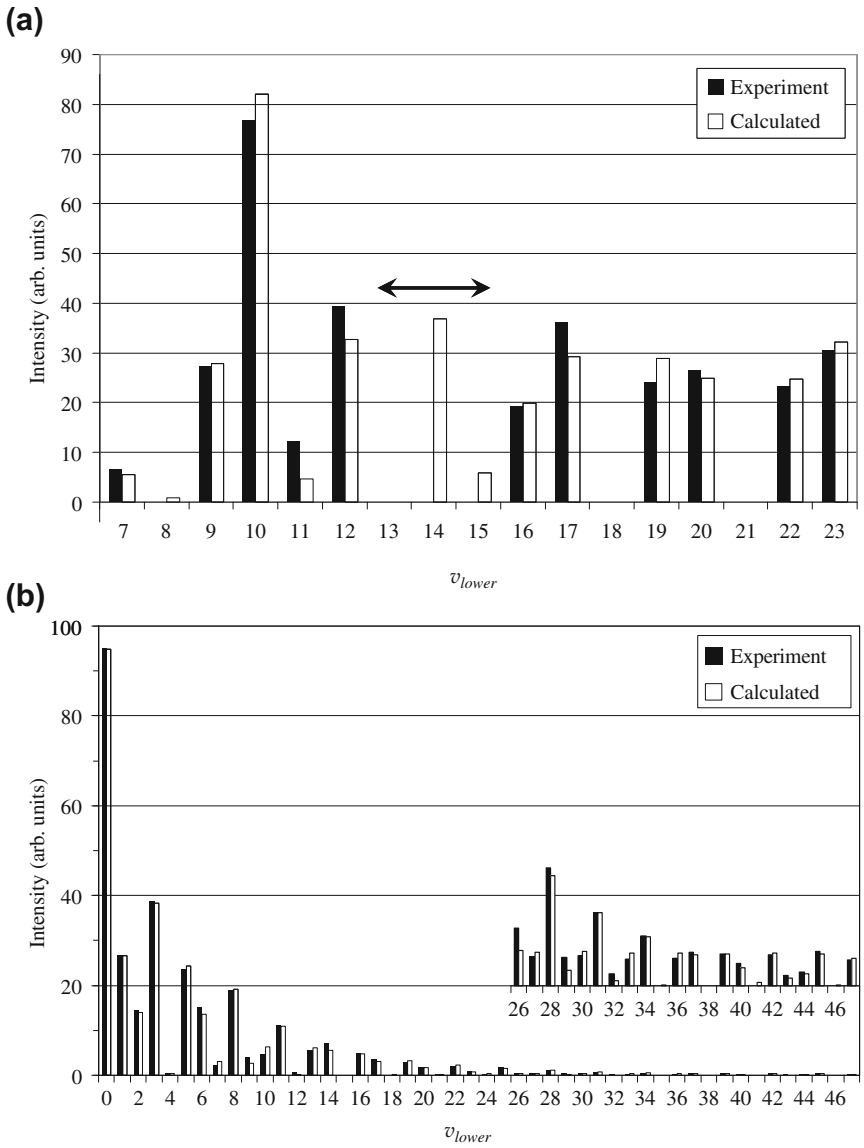

Figure 10 (a) Experimental and calculated intensities for NaK $3^1\Pi\ (19, 11, f) \rightarrow A^1\Sigma^+\ (v', 11, e)$ transitions. Transitions to $v_{\text{lower}} = v' = 13, 14,$ and 15, marked by a horizontal arrow, are unable to be used in the analysis, since light at these particular wavelengths experiences near-zero transmission through the vapor due to potassium resonance line absorption. (b) Experimental and fitted intensities for $3^1\Pi\ (19, 11, f) \rightarrow X^1\Sigma^+\ (v'', 11, e)$ transitions. $v_{\text{lower}} = v''$. Inset: intensities magnified by factor of 20 (Sweeney et al., 2008). Figure reprinted with permission from Sweeney et al. (2008). Copyright 2008 by the American Institute of Physics.

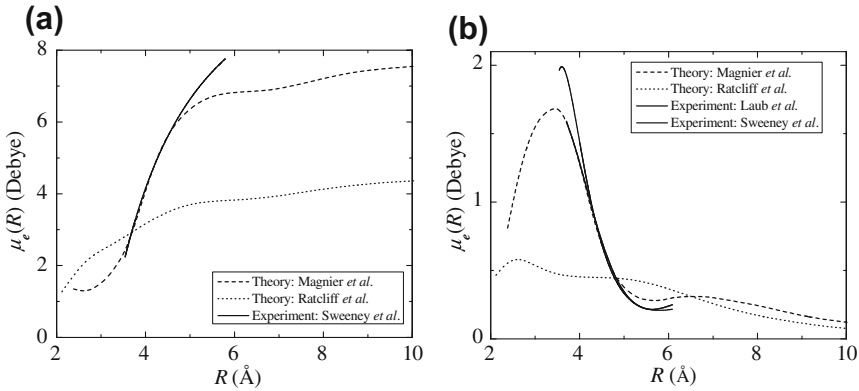

Figure 11 Solid line: absolute experimental transition dipole moment function versus internuclear separation for (a) the NaK $3^1\Pi \rightarrow A^1\Sigma^+$ transition, and (b) the NaK $3^1\Pi \rightarrow X^1\Sigma^+$ transition, both from Sweeney et al. (2008). The thin solid line in (b) is the relative transition dipole moment function from Laub et al. (1999), normalized to theory at R = 4.76 Å. In both (a) and (b), the dashed line is the theoretical transition dipole moment function from Magnier et al. (2000), and the dotted line is the theoretical transition dipole moment from Ratcliff et al. (1985). Figure reprinted with permission from Sweeney et al. (2008). Copyright 2008 by the American Institute of Physics.

4.4 AT Based Quantum Control of the Spin–Orbit Interaction

The spin–orbit interaction can mix molecular electronic states of different spin multiplicity, with the degree of mixing dependent on the spin–orbit matrix element as well as the energy separation between the interacting states. As discussed above, the AT effect causes energy levels to split and shift, thereby offering the possibility to change the separation between two interacting levels. Thus control of the spin–orbit mixing can be realized using a laser field as an external control mechanism. Several recent theoretical studies have been devoted to this subject (Gonzalez-Vazquez et al., 2006a, 2006b; Kirova & Spano, 2005; Korolkov & Manz, 2004) with a proof-of-concept experiment presented in Ahmed et al. (2011).

Specific possible applications of quantum control of the spin–orbit interaction include enhancing the rate of population transfer to otherwise "dark" states, either by increasing the mixing between existing perturbed pairs of levels, or by creating mixed levels out of previously unmixed ones. As mentioned previously, levels of alkali molecules with mixed singlet–triplet character are frequently used as "windows" for accessing higher lying triplet states (Li et al., 1992; Lyyra et al., 1991; Xie & Field, 1985), and as intermediate levels in the transfer of cold molecules formed at long range in the triplet $a^3\Sigma^+$ state to deeply bound levels of the singlet $X^1\Sigma^+$

ground state (Danzl et al., 2008; Ghosal et al., 2009; Ni et al., 2008; Sage et al., 2005; Viteau et al., 2008). Thus, the ability to enhance the mixing of the spin character of singlet–triplet pairs of states could be used to improve the transfer rates in such schemes. Additional applications are discussed in Ahmed et al. (2011).

All-optical control of the spin–orbit interaction was demonstrated in Ahmed et al. (2011) using the lithium dimer ($^7Li_2$) and a narrow band cw laser with moderate output power as the control field. The small linewidth (0.5 MHz) of the cw control laser allowed state selectively with a specific singlet–triplet pair of rovibrational levels mixed by the spin–orbit interaction. $^7Li_2$ was chosen for the proof-of-concept experiment since for molecules with light nuclei the spin and orbital angular momenta are weakly coupled and therefore the spin–orbit interaction is small. Thus interacting levels can lie very close in energy without being significantly mixed. As shown in Figure 12, the thermal population of level $|1\rangle$ was excited to level $|2\rangle$ by the weak pump laser L_1 at 15810.158 cm^{-1}, and then further excited by tuning the weak probe field L_2 to the mixed pair of levels $1^3\Sigma_g^-$ $(v = 1, N = 21, f) \sim G^1\Pi_g$ $(v = 12, J = 21, f)$, denoted as $|T\rangle$ and $|S\rangle$, with resonances at 17666.136 cm^{-1} and 17666.162 cm^{-1}, respectively. The strong control laser L_3 was set on resonance with the $G^1\Pi_g$ $(v = 12, J = 21, f) \leftrightarrow A^1\Sigma_u^+$ $(v' = 14, J' = 21, e)$ transition $(|S\rangle \leftrightarrow |3\rangle)$ at 17026.872 cm^{-1}. The $^7Li_2$ $G^1\Pi_g$ $(v = 12, J = 21, f) \sim 1^3\Sigma_g^-$ $(v = 1, N = 21, f)$ pair of rovibrational levels was chosen since the two levels are only separated by 750 MHz, as is evident from Figure 13, but still have very small natural mixing. In the absence of a control field, the nominally singlet (triplet) level has 87% singlet (triplet) and 13% triplet (singlet) character, determined using the ratios of the intensities from OODR laser excitation scans of the triplet and singlet peaks as described below. The $1^3\Sigma_g^-$ electronic state has negligible hyperfine structure (Yiannopoulou et al., 1994), and thus the predominantly triplet state $1^3\Sigma_g^-$ $(v = 1, N = 21, f)$ can be considered to be a single level in the analysis.

As in other experiments, $^7Li_2$ dimers were produced in a heat pipe oven operating at ~850 K with ~150 mTorr of argon buffer gas. Argon and lithium atom densities were sufficiently low that level changing collisions could be neglected. The excitation scheme (Figure 12) used three narrow band tunable ring dye lasers; the pump (L_1) and probe (L_2) lasers counter-propagated through the oven, while the control laser (L_3) co-propagated with the pump. The pump and probe laser powers were kept as low as possible while maintaining a good signal-to-noise ratio; $P(L_1) \approx 100$ μW and $P(L_2) \approx 2.5$ mW. The spot radii of the pump and probe lasers ($r_1 = 125$ μm and $r_2 = 130$ μm) were chosen to be about half that of the control laser ($r_3 = 230$ μm).

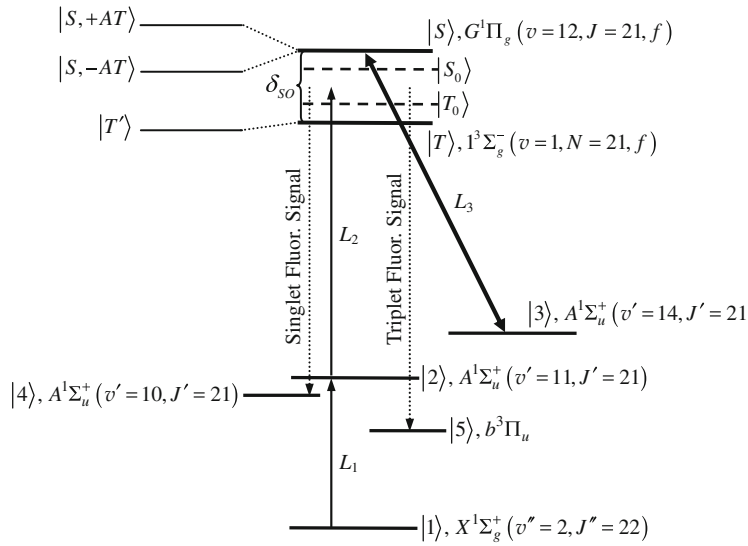

Figure 12 The thermal population in level $|1\rangle$ is excited to level $|2\rangle$ by the weak L_1 pump laser, and then further excited by the weak L_2 probe field to the mixed pair of levels $|T\rangle$ and $|S\rangle$. The strong L_3 control laser is set on resonance with the $|S\rangle \leftrightarrow |3\rangle$ transition. Levels $|S_0\rangle$ and $|T_0\rangle$ depicted with dashed lines represent the "pure" singlet and triplet basis states, respectively (unperturbed basis set). When the spin–orbit interaction is taken into account, levels $|S_0\rangle$ and $|T_0\rangle$ transform into the nominally singlet $|S\rangle$ and triplet $|T\rangle$ states. When the control laser is turned on, these states evolve further into, $|S,-AT\rangle$, $|S,+AT\rangle$, and $|T'\rangle$. Figure reprinted with permission from Ahmed et al. (2011). Copyright 2011 by the American Physical Society.

The spin character of the mixed pair of levels $|S\rangle \sim |T\rangle$ was observed by simultaneously recording fluorescence from them to lower lying singlet and triplet levels (see Figure 12). In order to monitor the triplet character, fluorescence to a few lower lying rovibrational levels of the $b^3\Pi_u$ electronic state (collectively labeled level $|5\rangle$ in Figure 12), was detected with a filtered PMT. The singlet character was monitored by observing fluorescence to a specific rovibrational level, $A^1\Sigma_u^+$ $(v'=10, J'=21)$ (level $|4\rangle$ in Figure 12), using a monochromator/PMT system as shown in Figure 5.

The density matrix formalism (see Section 2) was used to analyze the results. The Hamiltonian of the system can be expressed as the sum of three parts $H = H_{mol} + H_{int} + H_{SO}$. H_{mol} and H_{int} represent the Hamiltonian of the unperturbed molecule and the interaction of the molecule with the optical fields, respectively (see Section 2). Because the spin–orbit interaction in Li_2 ($\sim$0.1 cm^{-1}) is much smaller than the typical spacing between the individual rovibrational levels ($\sim$20 cm^{-1} at $J=20$) it can be assumed that H_{SO} mixes only the closely spaced pair of unperturbed pure singlet $|S_0\rangle$ and pure triplet $|T_0\rangle$ states (eigenstates of H_{mol}). The result of the spin–orbit

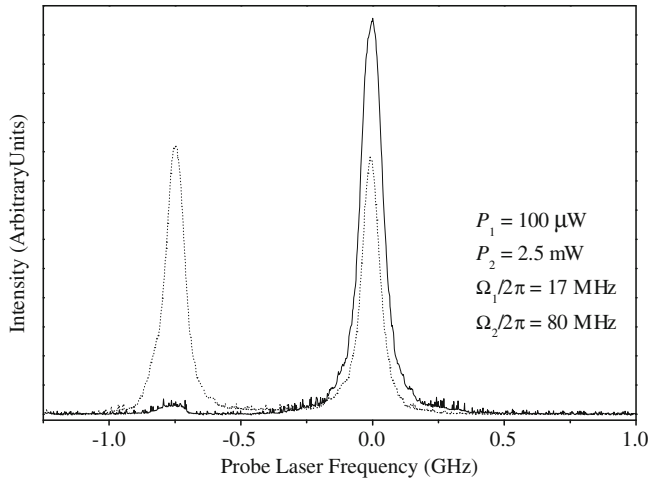

Figure 13 Optical–optical double resonance spectra recorded by monitoring the fluorescence to the $A^1\Sigma_u^+$ $(v' = 10, J' = 21)$ level (singlet channel—solid line) and to a few low lying rovibrational levels of the $b^3\Pi_u$ state (triplet channel—dotted line) as a function of the detuning of the probe laser. The control laser was blocked during these scans. From these spectra the separation of the singlet and triplet components of the perturbed pair $|S\rangle$ and $|T\rangle$ was found to be $\delta_{SO} = 750$ MHz in the absence of the control field. Probe laser frequencies here and in Figures 14 and 15 are relative to the frequency of the transition to the nominally singlet level $|S\rangle$ in the absence of the control laser. Figure reprinted with permission from Ahmed et al. (2011). Copyright 2011 by the American Physical Society.

perturbation, as shown in Figure 12, is the creation of the mixed states $|S\rangle$ and $|T\rangle$ given by $|S\rangle = \alpha|S_0\rangle - \beta|T_0\rangle$ and $|T\rangle = \alpha|T_0\rangle + \beta|S_0\rangle$, where α and β are mixing coefficients and $\alpha^2 + \beta^2 = 1$.

Values of α and β were determined from fluorescence ratios (in the absence of the coupling laser) as described in Sun and Huennekens (1992). Specifically, the triplet channel fluorescence signals originating from levels $|S\rangle$ and $|T\rangle$ depend on the populations of the upper levels ($n_{|S\rangle}$ and $n_{|T\rangle}$) and the Einstein A coefficients for the respective transitions; i.e.,

$$I(t)_{|S\rangle} = \varepsilon_t \nu_t^4 |\langle S|\mu_e^t(R)|b^3\Pi_u\rangle|^2 n_{|S\rangle} = \varepsilon_t \nu_t^4 \beta^2 |\langle T_0|\mu_e^t(R)|5\rangle|^2 n_{|S\rangle} \tag{35}$$

and

$$I(t)_{|T\rangle} = \varepsilon_t \nu_t^4 |\langle T|\mu_e^t(R)|b^3\Pi_u\rangle|^2 n_{|T\rangle} = \varepsilon_t \nu_t^4 \alpha^2 |\langle T_0|\mu_e^t(R)|5\rangle|^2 n_{|T\rangle}, \tag{36}$$

where $|b^3\Pi_u\rangle \equiv |5\rangle$ represents the specific low lying rovibrational levels of the $b^3\Pi_u$ state that are accessible from levels $|S\rangle$ and $|T\rangle$ by fluorescence photons within the bandpass of the triplet fluorescence channel filters, ν_t is the average frequency, and ε_t is the total detection system efficiency for

detection of these photons. Here it is assumed that fluorescence to the $b^3\Pi_u$ state from the pure singlet state $|S_0\rangle$ is forbidden by the dipole selection rules on spin. Similarly, the singlet channel fluorescence signals are given by

$$\begin{aligned} I(s)_{|S\rangle} &= \varepsilon_s \nu_s^4 |\langle S|\mu_e^s(R)|A^1\Sigma_u^+ \ (v'=10, J'=21)\rangle|^2 n_{|S\rangle} \\ &= \varepsilon_s \nu_s^4 \alpha^2 |\langle S_0|\mu_e^s(R)|4\rangle|^2 n_{|S\rangle} \end{aligned} \tag{37}$$

and

$$\begin{aligned} I(s)_{|T\rangle} &= \varepsilon_s \nu_s^4 |\langle T|\mu_e^s(R)|A^1\Sigma_u^+ \ (v'=10, J'=21)\rangle|^2 n_{|T\rangle} \\ &= \varepsilon_s \nu_s^4 \beta^2 |\langle S_0|\mu_e^s(R)|4\rangle|^2 n_{|T\rangle}. \end{aligned} \tag{38}$$

Defining $\varepsilon \equiv \left(\varepsilon_s \nu_s^4 |\langle S_0|\mu_e^s(R)|4\rangle|^2\right)/\left(\varepsilon_t \nu_t^4 |\langle T_0|\mu_e^t(R)|5\rangle|^2\right)$ we see that the ratios of singlet to triplet fluorescence from each of the upper levels are given by

$$\frac{I(s)_{|S\rangle}}{I(t)_{|S\rangle}} = \varepsilon \frac{\alpha^2}{\beta^2} \tag{39}$$

and

$$\frac{I(s)_{|T\rangle}}{I(t)_{|T\rangle}} = \varepsilon \frac{\beta^2}{\alpha^2}. \tag{40}$$

Thus all factors of populations, matrix elements, frequencies, and efficiency factors cancel out in the ratio of the ratios

$$\frac{I(s)_{|S\rangle}/I(t)_{|S\rangle}}{I(s)_{|T\rangle}/I(t)_{|T\rangle}} = \frac{\alpha^4}{\beta^4}. \tag{41}$$

From this analysis, it was determined in Ahmed et al. (2011) that $\alpha^2 = 0.87$ and $\beta^2 = 0.13$ for the $^7Li_2$ pair of levels $G^1\Pi_g$ $(v = 12, J = 21, f) \sim 1^3\Sigma_g^-$ $(v = 1, N = 21, f)$.

The spin–orbit interaction part of the Hamiltonian of the system, H_{SO}, can be expressed simply as $H_{SO} = \alpha\beta\delta_{SO}$, where δ_{SO} is the separation in energy between the mixed levels $|S\rangle$ and $|T\rangle$.

In the interaction picture, the Hamiltonian, H_I, of the system in this case, after applying the rotating wave approximation, has the explicit form:

$$\begin{aligned} H_I = &-\hbar\delta_1|2\rangle\langle 2| - \hbar(\delta_1+\delta_2)|S_0\rangle\langle S_0| - \hbar(\delta_1+\delta_2-\delta_3)|3\rangle\langle 3| \\ &- \hbar(\delta_1+\delta_2+\delta_{SO}^0)|T_0\rangle\langle T_0| + \frac{\hbar\Omega_1}{2}(|2\rangle\langle 1| + |1\rangle\langle 2|) \\ &+ \frac{\hbar\Omega_2}{2}(|S_0\rangle\langle 2| + |2\rangle\langle S_0|) + \frac{\hbar\Omega_3}{2}(|3\rangle\langle S_0| + |S_0\rangle\langle 3|) \\ &+ \hbar\alpha\beta\delta_{SO}(|S_0\rangle\langle T_0| + |T_0\rangle\langle S_0|) \end{aligned} \tag{42}$$

in a basis of levels that are unperturbed by either the optical fields or the spin–orbit interaction. δ_{SO}^0 is the splitting of the unperturbed levels [note $\delta_{SO}^0 = (\alpha^2 - \beta^2)\delta_{SO}$ where δ_{SO} is the measurable separation between the mixed levels $|S\rangle$ and $|T\rangle$ with no control laser].

With only the weak pump and probe lasers present, the laser interactions are minimal, and the upper levels are essentially the perturbed spin–orbit pair $|S\rangle$ and $|T\rangle$. The fluorescence excitation spectrum of the $|S\rangle \sim |T\rangle$ system as a function of the probe laser detuning shows a two peak pattern as expected (see Figure 13).

When the control field is turned on, resonantly coupling states $|S\rangle$ and $|3\rangle$, the nominally singlet peak is observed to split into two components due to the AT effect as shown in Figure 14. The separation between the two components, labeled $|S,-AT\rangle$ and $|S,+AT\rangle$, of the upper split singlet peak is determined by the Rabi frequency of the control laser. The $|S,-AT\rangle$ component of the pair is shifted closer to the nearby $|T\rangle$ state which leads to stronger spin–orbit interaction between them. As a result, the $|S,-AT\rangle$ component acquires more triplet character, while the $|T\rangle$ level shifts slightly and acquires more singlet character, being transformed into the modified state $|T'\rangle$. This is demonstrated by the significant increase in the area of the $1^3\Sigma_g^-$ $(v=1, N=21, f)$ peak in the singlet detection channel as can be seen in Figure 14b. At the same time the singlet character of the $|S,+AT\rangle$ component is enhanced due to its increased separation from the $|T\rangle$ state (which decreases its mixing with the triplet level). The two AT split components of the predominantly singlet level now have different amounts of singlet and triplet character from each other. This results in an asymmetric line shape of the AT pair intensity distribution, in both the singlet and triplet detection channels, as is evident from Figure 14a.

To estimate how the character of the nominally triplet level $1^3\Sigma_g^-$ $(v=1, N=21, f)$ changes in the presence of the control laser, state $|T'\rangle$ is assumed to be a superposition of the unperturbed levels $|T_0\rangle$, $|S_0\rangle$, and $|3\rangle$; i.e., $|T'\rangle = \alpha'|T_0\rangle + \beta'|S_0\rangle + \gamma'|3\rangle$, where α', β', and γ' are the mixing coefficients with the control laser on. The spin–orbit interaction only mixes $|T_0\rangle$ with $|S_0\rangle$ but not with $|3\rangle$ due to the spin–orbit selection rules ($g \nleftrightarrow u$, and $\Delta J = 0$). Thus the mixing of level $|3\rangle$ character into state $|T'\rangle$

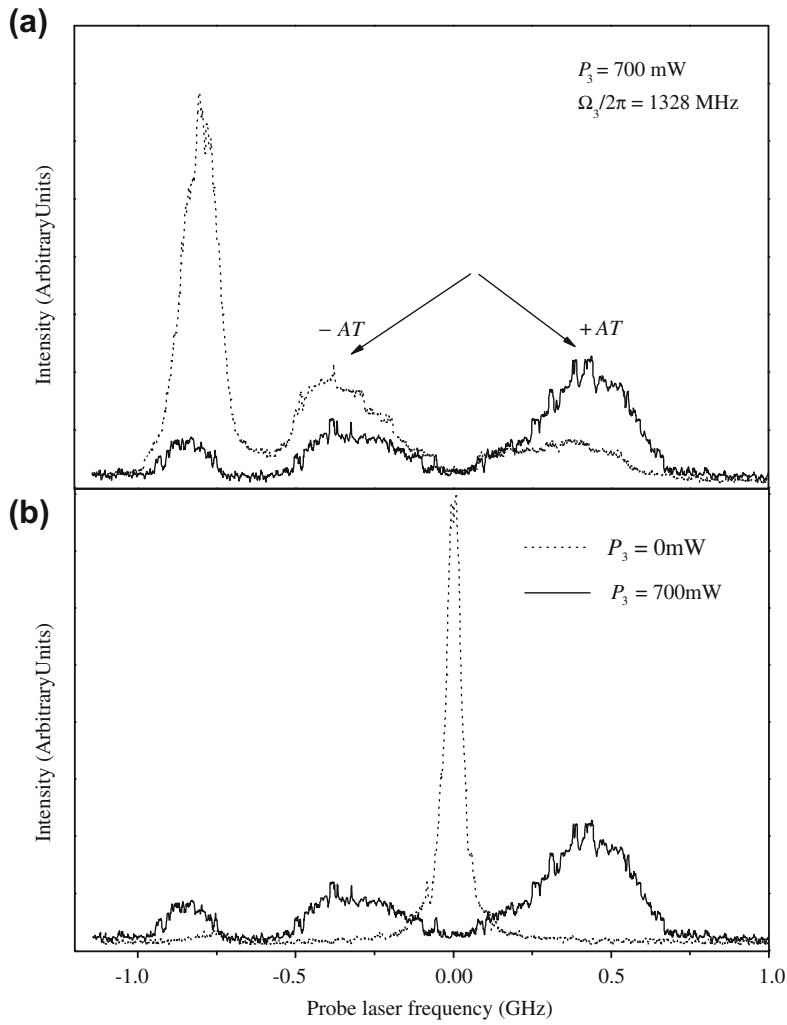

Figure 14 (a) The singlet (solid line) and triplet (dotted line) channel spectra recorded simultaneously in the presence of the control laser. Since the $|S, -AT\rangle$ component has acquired more triplet character (and the $|S, +AT\rangle$ component has lost triplet character) their intensities are asymmetric in opposite directions for the singlet and triplet signals. The parameters for L_1 and L_2 were the same as in Figure 13. (b) Comparison of the singlet detection channel spectra with ($P_3 = 700$ mW) and without ($P_3 = 0$ mW) the control laser. It can be seen that the singlet character of the predominantly triplet level $1^3\Sigma_g^-$ $(v = 1, N = 21, f)$ is dramatically enhanced by the presence of the control laser. Figure reprinted with permission from Ahmed et al. (2011). Copyright 2011 by the American Physical Society.

only occurs via the relatively small $\beta'|S_0\rangle$ component in the latter. Consequently in the simple model of Ahmed et al. (2011), γ' was set to 0. Using $I(s)_{|T'\rangle}/I(t)_{|T'\rangle} = \varepsilon(\beta')^2/(\alpha')^2$, where $I(s)_{|T'\rangle}$ and $I(t)_{|T'\rangle}$ are the singlet and triplet channel fluorescence intensities (peak areas) of state $|T'\rangle$ in Figure 14a, the normalization condition $(\alpha')^2 + (\beta')^2 = 1$, ε from Equation (39) or (40), and the data from Figure 13, these authors obtained the values $(\alpha')^2 = 0.72$ and $(\beta')^2 = 0.28$. A comparison of β^2 and $(\beta')^2$ indicates that the singlet character of the nominally triplet state was enhanced by more than a factor of two, from 13% to 28%, when the control laser with power of 700 mW was turned on.

By varying the amplitude of the control laser field one can enhance or reduce the spin–orbit interaction. The control effect depends on the magnitude of the induced shift in the position of the levels relative to the natural spin–orbit splitting δ_{SO}. Figure 15 shows probe laser scans with

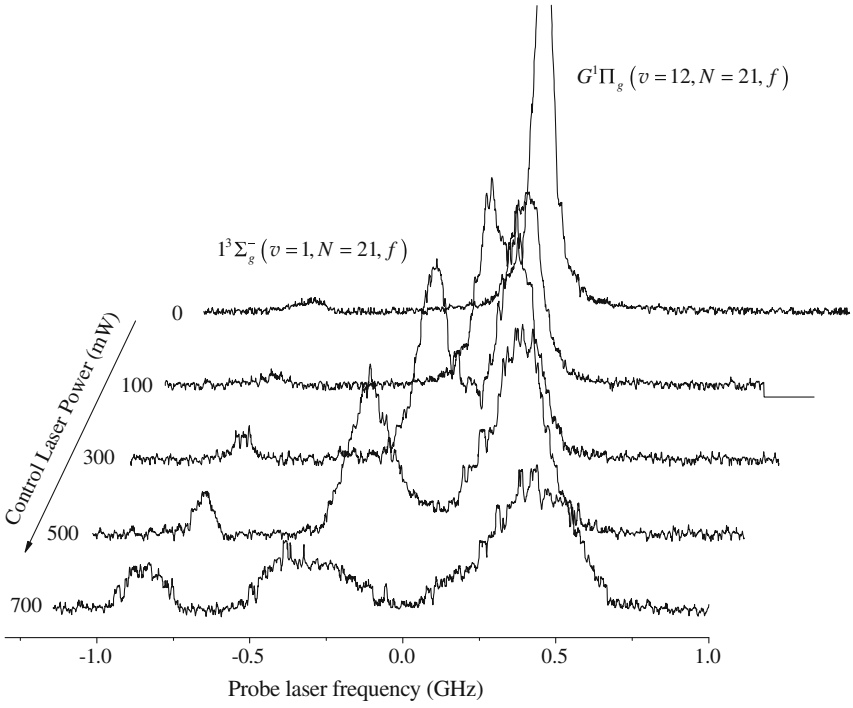

Figure 15 Dependence of the singlet–triplet mixing and the magnitude of the AT splitting on the control laser power. The spectra were recorded by monitoring singlet fluorescence down to the $A^1\Sigma_u^+$ $(v' = 10, J' = 21)$ level. The leftmost peak in each spectrum corresponds to fluorescence from the level $|T'\rangle$ with primarily $1^3\Sigma_g^-$ $(v = 1, N = 21, f)$ character, while the peak(s) on the right correspond to fluorescence from the AT split pair of levels $|S, -AT\rangle$ and $|S, +AT\rangle$ with primarily $G^1\Pi_g$ $(v = 12, J = 21, f)$ character. Figure reprinted with permission from Ahmed et al. (2011). Copyright 2011 by the American Physical Society.

detection of the singlet fluorescence for a number of power levels of the control laser. At low power values (100 mW), there is no measurable enhancement of the mixing and the AT split components are symmetric. Increasing the control laser power leads to an increase in the mixing. The nominally $1^3\Sigma_g^-$ $(v = 1, N = 21, f)$ peak grows in the singlet detection channel and the AT split pair of peaks becomes more and more asymmetric. At higher control laser powers (500–700 mW) a shift in the position as well as broadening of the $1^3\Sigma_g^-$ $(v = 1, N = 21, f)$ peak can be observed due to the nonresonant AC-Stark effect of the control laser and the increased spin–orbit interaction of $|T'\rangle$ with the $|S, -AT\rangle$ component.

5. CONCLUSIONS

This review has focused on novel frequency domain applications of the Autler–Townes effect in molecular systems. We have described how this coherent effect can be used as a precision probe of the internuclear distance dependent molecular transition dipole moment function, a parameter of fundamental importance in the interaction of light with matter. This application relies on an accurate measurement of the electric field amplitude of the coupling laser and a determination of the Rabi frequency from the Autler–Townes split line shape in the probe laser scan.

We have also attempted to highlight the power of the Autler–Townes effect as a quantum control mechanism of the molecular angular momentum alignment and the spin–orbit interaction. In the former case, the ability to align and orient molecules along a lab-fixed axis prior to a chemical reaction is essential for understanding how relative orientations influence reaction dynamics. In the latter case, the Autler–Townes splitting provides a "control knob" for "tuning" the spin–orbit mixing coefficients of a pair of weakly mixed singlet and triplet states. This mechanism can be used as a powerful tool for controlling molecular valence electron spin polarization. The change in magnitude of the spin–orbit interaction depends on the Rabi frequency (laser power) of the control laser. The quantum state electron spin control can also be extended to experiments with stronger control fields, bearing in mind that the control laser does not need to be resonant with a populated ground state level. This feature is particularly useful for mitigating the effects of multi-photon ionization in such experiments. In addition, by combining the quadruple resonance technique with the spin–orbit mixing control scheme, it might be possible to enhance state selected ultracold molecule formation in the molecular ground state of alkali diatomic molecules starting from a triplet ground state Feshbach resonance. Control of the spin–orbit interaction, and thereby of the valence electron spin polarization, can also be used to probe the role of electron spin in reactive photochemistry.

ACKNOWLEDGMENTS

We gratefully acknowledge valuable discussions with Dr. F. C. Spano on the development of the theoretical model. We also acknowledge the valuable contributions of our co-workers Dr. Omer Salihoglu, Dr. Sonja Ingram, Dr. Peng Qi, Dr. Steven Sweeney, Yafei Guan, and Prof. Svetlana Kotochigova. We are grateful for financial support from NSF Grant Nos. PHY-0555608, PHY-0855502, PHY-0652938, and PHY-0968898.

REFERENCES

Ahmed, E., Hansson, A., Qi, P., Kirova, T., Lazoudis, A., Kotochigova, S., Lyyra, A. M., Li, L., Qi, J., & Magnier, S. (2006). Measurement of the electronic transition dipole moment by Autler–Townes splitting: Comparison of three- and four-level excitation schemes for the Na_2 $A^1\Sigma_u^+$–$X^1\Sigma_g^+$ system. *Journal of Chemical Physics, 124*, 084308.

Ahmed, E. H., Ingram, S., Kirova, T., Salihoglu, O., Huennekens, J., Qi, J., Guan, Y., & Lyyra, A. M. (2011). Quantum control of the spin–orbit interaction using the Autler–Townes effect. *Physical Review Letters, 107*, 163601.

Ahmed, E., & Lyyra, A. M. (2007). Effect of Doppler broadening on Autler–Townes splitting in the molecular cascade excitation scheme. *Physical Review A, 76*, 053407.

Ahmed, E. H., Qi, P., Beser, B., Bai, J., Field, R. W., Huennekens, J. P., & Lyyra, A. M. (2008). Experimental mapping of the absolute magnitude of the transition dipole moment function μ_e (R) of the Na_2 $A^1\Sigma_u^+ - X^1\Sigma_g^+$ transition. *Physical Review A, 77*, 053414.

Ahmed, E. H., Qi, P., & Lyyra, A. M. (2009). All-optical cw quadruple resonance excitation: A coherently driven five-level molecular system. *Physical Review A, 79*, 062509.

Alzetta, G., Gozzini, A., Moi, L., & Orriols, G. (1976). Experimental-method for observation of RF transitions and laser beat resonances in oriented Na vapor. *Nuovo Cimento Della Societa Italiana Di Fisica B – General Physics Relativity Astronomy and Mathematical Physics and Methods, 36*, 5–20.

Arimondo, E. (1995). *Progress in optics*. Amsterdam: Elsevier.

Arimondo, E., & Orriols, G. (1976). Nonabsorbing atomic coherences by coherent 2-photon transitions in a 3-level optical-pumping. *Lettere Al Nuovo Cimento, 17*, 333–338.

Ates, C., Sevincli, S., & Pohl, T. (2011). Electromagnetically induced transparency in strongly interacting Rydberg gases. *Physical Review A, 83*, 041802.

Atherton, P. S., Dalton, B. J., & Dagg, I. R. (1986). Autler–Townes doublets in the hyperfine transitions of $^{14}NH_3$. *Journal of Physics B – Atomic Molecular and Optical Physics, 19*, 277–292.

Autler, S. H., & Townes, C. H. (1955). Stark effect in rapidly varying fields. *Physical Review, 100*, 703–722.

Baur, M., Filipp, S., Bianchetti, R., Fink, J. M., Goeppl, M., Steffen, L., Leek, P. J., Blais, A., & Wallraff, A. (2009). Measurement of Autler–Townes and Mollow transitions in a strongly driven superconducting qubit. *Physical Review Letters, 102*, 243602.

Benabid, F., Antonopoulos, G., Knight, J. C., & Russell, P. S. (2005a). Stokes amplification regimes in quasi-cw pumped hydrogen-filled hollow-core photonic crystal fiber. *Physical Review Letters, 95*, 213903.

Benabid, F., Couny, F., Knight, J. C., Birks, T. A., & Russell, P. S. (2005b). Compact, stable and efficient all-fibre gas cells using hollow-core photonic crystal fibres. *Nature, 434*, 488–491.

Benabid, F., Light, P. S., Couny, F., & Russell, P. S. (2005c). Electromagnetically-induced transparency grid in acetylene-filled hollow-core PCF. *Optics Express, 13*, 5694–5703.

Bergmann, K., Theuer, H., & Shore, B. W. (1998). Coherent population transfer among quantum states of atoms and molecules. *Reviews of Modern Physics, 70*, 1003–1025.

Boller, K. J., Imamoglu, A., & Harris, S. E. (1991). Observation of electromagnetically induced transparency. *Physical Review Letters, 66*, 2593–2596.

Boon, J. R., Zekou, E., Mcgloin, D., & Dunn, M. H. (1999). Comparison of wavelength dependence in cascade-, Lambda-, and Vee-type schemes for electromagnetically induced transparency. *Physical Review A, 59*, 4675–4684.

Cohen-Tannoudji, C., Dupont-Roc, J., & Grynberg, G. (2004). *Atom–photon interactions*. Weinheim: Wiley-VCH.

Cohen-Tannoudji, C., & Reynaud, S. (1977). Dressed-atom description of resonance fluorescence and absorption-spectra of a multilevel atom in an intense laser-beam. *Journal of Physics B – Atomic Molecular and Optical Physics, 10*, 345–363.

Condon, E. U. (1928). Nuclear motions associated with electron transitions in diatomic molecules. *Physical Review, 32*, 858.

Danzl, J. G., Haller, E., Gustavsson, M., Mark, M. J., Hart, R., Bouloufa, N., Dulieu, O., Ritsch, H., & Nagerl, H. C. (2008). Quantum gas of deeply bound ground state molecules. *Science, 321*, 1062–1066.

Danzl, J. G., Mark, M. J., Haller, E., Gustavsson, M., Hart, R., Liem, A., Zellmer, H., & Nagerl, H. C. (2009). Deeply bound ultracold molecules in an optical lattice. *New Journal of Physics, 11*, 055036.

Deiglmayr, J., Grochola, A., Repp, M., Mortlbauer, K., Gluck, C., Lange, J., Dulieu, O., Wester, R., & Weidemuller, M. (2008). Formation of ultracold polar molecules in the rovibrational ground state. *Physical Review Letters, 101*, 133004.

Delsart, C., & Keller, J. C. (1976). Observation of optical Autler–Townes splitting in neon gas with a cascade level scheme. *Journal of Physics B – Atomic Molecular and Optical Physics, 9*, 2769–2775.

Durr, S., Volz, T., Marte, A., & Rempe, G. (2004). Observation of molecules produced from a Bose–Einstein condensate. *Physical Review Letters, 92*, 020406.

Fano, U. (1961). Effects of configuration interaction on intensities and phase shifts. *Physical Review, 124*, 1866–1878.

Fraser, P. A. (1954). A method for determining the electronic transition moment for diatomic molecules. *Canadian Journal of Physics, 32*, 515–521.

Friedrich, B., Slenczka, A., & Herschbach, D. (1994). Hybridization of rotor states in parallel electric and magnetic fields. *Chemical Physics Letters, 221*, 333–340.

Fulton, D. J., Shepherd, S., Moseley, R. R., Sinclair, B. D., & Dunn, M. H. (1995). Continuous-wave electromagnetically induced transparency—A comparison of V-system, Lambda-system, and cascade systems. *Physical Review A, 52*, 2302–2311.

Garcia-Fernandez, R., Ekers, A., Klavins, J., Yatsenko, L. P., Bezuglov, N. N., Shore, B. W., & Bergmann, K. (2005). Autler–Townes effect in a sodium molecular-ladder scheme. *Physical Review A, 71*, 023401.

Gerstenkorn, S., & Luc, P. (1978). *Atlas du Spectre d'Absorption de la Molecule d'Iode*, Paris.

Gerstenkorn, S., & Luc, P. (1979). Absolute iodine (I2) standards measured by means of Fourier-transform spectroscopy. *Revue De Physique Appliquee, 14*, 791–794.

Ghosal, S., Doyle, R. J., Koch, C. P., & Hutson, J. M. (2009). Stimulating the production of deeply bound RbCs molecules with laser pulses: The role of spin–orbit coupling in forming ultracold molecules. *New Journal of Physics, 11*, 055011.

Ghosh, S., Sharping, J. E., Ouzounov, D. G., & Gaeta, A. L. (2005). Resonant optical interactions with molecules confined in photonic band-gap fibers. *Physical Review Letters, 94*, 093902.

Girard, B., Billy, N., Vigue, J., & Lehmann, J. C. (1983). Evidence for a dynamical Stark effect in CO ($A^1\Pi$) two-photon excitation. *Chemical Physics Letters, 102*, 168–173.

Girard, B., Sitz, G. O., Zare, R. N., Billy, N., & Vigue, J. (1992). Polarization dependence of the AC Stark effect in multiphoton transitions of diatomic molecules. *Journal of Chemical Physics, 97*, 26–41.

Gonzalez-Vazquez, J., Sola, I. R., Santamaria, J., & Malinovsky, V. S. (2006a). Optical control of the singlet–triplet transition in Rb_2. *Journal of Chemical Physics, 125*, 124315.

Gonzalez-Vazquez, J., Sola, I. R., Santamaria, J., & Malinovsky, V. S. (2006b). Quantum control of spin–orbit coupling by dynamic Stark-shifts induced by laser fields. *Chemical Physics Letters, 431*, 231–235.

Gray, H. R., & Stroud, C. R. (1978). Autler–Townes effect in double optical resonance. *Optics Communications, 25*, 359–362.

Greiner, M., Regal, C. A., & Jin, D. S. (2003). Emergence of a molecular Bose–Einstein condensate from a Fermi gas. *Nature, 426*, 537–540.

Han, D. G., Guo, H., Bai, Y. F., & Sun, H. (2005). Subluminal and superluminal propagation of light in an N-type medium. *Physics Letters A, 334*, 243–248.

Harris, S. E. (1997). Electromagnetically induced transparency. *Physics Today, 50*, 36–42.

Harris, S. E., Field, J. E., & Imamoglu, A. (1990). Nonlinear optical processes using electromagnetically induced transparency. *Physical Review Letters, 64*, 1107–1110.

Herzberg, G. H. (1950). *Molecular spectra and molecular structure. I. Spectra of diatomic molecules*. Princeton: D. Van Nostrand.

Huo, W. M., Gross, K. P., & Mckenzie, R. L. (1985). Optical Stark effect in the two-photon spectrum of NO. *Physical Review Letters, 54*, 1012–1015.

Ichimura, K., Yamamoto, K., & Gemma, N. (1998). Evidence for electromagnetically induced transparency in a solid medium. *Physical Review A, 58*, 4116–4120.

Joshi, A., & Xiao, M. (2003). Electromagnetically induced transparency and its dispersion properties in a four-level inverted-Y atomic system. *Physics Letters A, 317*, 370–377.

Joshi, A., & Xiao, M. (2005). Generalized dark-state polaritons for photon memory in multilevel atomic media. *Physical Review A, 71*, R041801.

Karpa, L., Vewinger, F., & Weitz, M. (2008). Resonance beating of light stored using atomic spinor polaritons. *Physical Review Letters, 101*, 170406.

Kirova, T., & Spano, F. C. (2005). Designing molecular eigenstates in a four-level Λ system. *Physical Review A, 71*, 063816.

Knight, P. L., & Milonni, P. W. (1980). The Rabi frequency in optical-spectra. *Physics Reports – Review Section of Physics Letters, 66*, 21–107.

Korolkov, M. V., & Manz, J. (2004). Coherent spin control of matrix isolated molecules by IR plus UV laser pulses: Quantum simulations for CIF in Ar. *Journal of Chemical Physics, 120*, 11522–11531.

Kowalski, K., Long, V. C., Viet, H. N., Gateva, S., Glodz, M., & Szonert, J. (2009). Simultaneous coupling of three hfs components in a cascade scheme of EIT in cold ^{85}Rb atoms. *Journal of Non-Crystalline Solids, 355*, 1295–1301.

Kuklinski, J. R., Gaubatz, U., Hioe, F. T., & Bergmann, K. (1989). Adiabatic population transfer in a 3-level system driven by delayed laser-pulses. *Physical Review A, 40*, 6741–6744.

Laub, E., Mazsa, I., Webb, S. C., La Civita, J., Prodan, I., Jabbour, Z. J., Namiotka, R. K. & Huennekens, J. (1999). Experimental study of the NaK $3^1\Pi$ state. *Journal of Molecular Spectroscopy, 193*, 376–388. Erratum (2003). *Journal of Molecular Spectroscopy, 221*, 142–144.

Lazoudis, A., Ahmed, E. H., Li, L., Kirova, T., Qi, P., Hansson, A., Magnes, J., & Lyyra, A. M. (2008). Experimental observation of the dependence of Autler–Townes splitting on the probe and coupling laser wave-number ratio in Doppler-broadened open molecular cascade systems. *Physical Review A, 78*, 043405.

Lazoudis, A., Kirova, T., Ahmed, E. H., Li, L., Qi, J., & Lyyra, A. M. (2010). Electromagnetically induced transparency in an open Λ-type molecular lithium system. *Physical Review A, 82*, 023812.

Lazoudis, A., Kirova, T., Ahmed, E. H., Qi, P., Huennekens, J., & Lyyra, A. M. (2011). Electromagnetically induced transparency in an open V-type molecular system. *Physical Review A, 83*, 063419.

Lefebvre-Brion, H., & Field, R. W. (2004). *The spectra and dynamics of diatomic molecules*. Amsterdam: Elsevier.

Le Roy, R. J. (2007). *Level 8.0: A computer program for solving the radial Schrödinger equation for bound and quasibound levels*. University of Waterloo Chemical Physics Research Report No. CP663

Levine, R. D., & Bernstein, R. B. (1974). *Molecular reaction dynamics*. New York: Oxford University Press.

Li, H., Chen, H., Gubin, M. A., Rostovtsev, Y. V., Sautenkov, V. A., & Scully, M. O. (2010). Observation of electromagnetically induced transparency in cesium molecules. *Laser Physics, 20*, 1725–1728.

Li, L., Qi, P., Lazoudis, A., Ahmed, E., & Lyyra, A. M. (2005). Observation of electromagnetically induced transparency in two-photon transitions of $^{39}K_2$. *Chemical Physics Letters, 403*, 262–267.

Li, L., Zhu, Q. S., Lyyra, A. M., Whang, T. J., Stwalley, W. C., Field, R. W., & Alexander, M. H. (1992). Collision-induced transitions between A $^1\Sigma_u^+$ and b $^3\Pi_u$ states of Na_2—The gateway effect of perturbed levels. *Journal of Chemical Physics, 97*, 8835–8841.

Light, P. S., Benabid, F., Pearce, G. J., Couny, F., & Bird, D. M. (2009). Electromagnetically induced transparency in acetylene molecules with counterpropagating beams in V and Lambda schemes. *Applied Physics Letters, 94*, 141103.

Linskens, A. F., Dam, N., Reuss, J., & Sartakov, B. (1994). Alignment and orientation of nonpolar molecules utilizing the laser-induced AC-Stark effect. *Journal of Chemical Physics, 101*, 9384–9394.

Loesch, H. J., & Remscheid, A. (1990). Brute force in molecular reaction dynamics: A novel technique for measuring steric effects. *Journal of Chemical Physics, 93*, 4779–4790.

Lyyra, A. M., Wang, H., Whang, T. J., Stwalley, W. C., & Li, L. (1991). CW all-optical triple resonance spectroscopy. *Physical Review Letters, 66*, 2724–2727.

Magnier, S., Aubert-Frecon, M., & Millie, P. (2000). Potential energies, permanent and transition dipole moments for numerous electronic excited states of NaK. *Journal of Molecular Spectroscopy, 200*, 96–103.

Mitchell, A. C. G., & Zemansky, M. W. (1971). *Resonance radiation and excited atoms* . Cambridge, UK: Cambridge University Press.

Mohapatra, A. K., Bason, M. G., Butscher, B., Weatherill, K. J., & Adams, C. S. (2008). A giant electro-optic effect using polarizable dark states. *Nature Physics, 4*, 890–894.

Muller, A., Flagg, E. B., Bianucci, P., Wang, X. Y., Deppe, D. G., Ma, W., Zhang, J., Salamo, G. J., Xiao, M., & Shih, C. K. (2007). Resonance fluorescence from a coherently driven semiconductor quantum dot in a cavity. *Physical Review Letters, 99*, 187402.

Ni, K. K., Ospelkaus, S., De Miranda, M. H. G., Pe'er, A., Neyenhuis, B., Zirbel, J. J., Kotochigova, S., Julienne, P. S., Jin, D. S., & Ye, J. (2008). A high phase-space-density gas of polar molecules. *Science, 322*, 231–235.

Noda, C., & Zare, R. N. (1982). Relation between classical and quantum formulations of the Franck–Condon principle—The generalized *R*-centroid approximation. *Journal of Molecular Spectroscopy, 95*, 254–270.

Ospelkaus, C., Ospelkaus, S., Humbert, L., Ernst, P., Sengstock, K., & Bongs, K. (2006). Ultracold heteronuclear molecules in a 3D optical lattice. *Physical Review Letters, 97*, 120402.

Phillips, M. C., Wang, H. L., Rumyantsev, I., Kwong, N. H., Takayama, R., & Binder, R. (2003). Electromagnetically induced transparency in semiconductors via biexciton coherence. *Physical Review Letters, 91*, 183602.

Picque, J. L., & Pinard, J. (1976). Direct observation of Autler–Townes effect in optical range. *Journal of Physics B – Atomic Molecular and Optical Physics, 9*, L77–L81.

Pritchard, J. D., Maxwell, D., Gauguet, A., Weatherill, K. J., Jones, M. P. A., & Adams, C. S. (2010). Cooperative atom–light interaction in a blockaded Rydberg ensemble. *Physical Review Letters, 105*, 193603.

Qi, J., Lazarov, G., Wang, X. J., Li, L., Narducci, L. M., Lyyra, A. M., & Spano, F. C. (1999). Autler–Townes splitting in molecular lithium: Prospects for all-optical alignment of nonpolar molecules. *Physical Review Letters, 83*, 288–291.

Qi, J., & Lyyra, A. M. (2006). Electromagnetically induced transparency and dark fluorescence in a cascade three-level diatomic lithium system. *Physical Review A, 73*, 043810.

Qi, J., Spano, F. C., Kirova, T., Lazoudis, A., Magnes, J., Li, L., Narducci, L. M., Field, R. W., & Lyyra, A. M. (2002). Measurement of transition dipole moments in lithium dimers using electromagnetically induced transparency. *Physical Review Letters, 88*, 173003.

Quesada, M. A., Lau, A. M. F., Parker, D. H., & Chandler, D. W. (1987). Observation of Autler–Townes splitting in the multiphoton ionization of H_2: Measurement of vibronic transition moments between excited electronic states. *Physical Review A, 36*, 4107–4110.

Ratcliff, L. B., Konowalow, D. D., & Stevens, W. J. (1985). Electronic transition dipole moment functions for NaK. *Journal of Molecular Spectroscopy, 110*, 242–255.

Regal, C. A., Ticknor, C., Bohn, J. L., & Jin, D. S. (2003). Creation of ultracold molecules from a Fermi gas of atoms. *Nature, 424*, 47–50.

Ross, A. J., Clements, R. M., & Barrow, R. F. (1988). The $A(2)^1\Sigma^+$ state of NaK. *Journal of Molecular Spectroscopy, 127*, 546–548.

Russier-Antoine, I., Ross, A. J., Aubert-Frecon, M., Martin, F., & Crozet, P. (2000). An improved potential energy curve for the ground state of NaK. *Journal of Physics B – Atomic Molecular and Optical Physics, 33*, 2753–2762.

Sage, J. M., Sainis, S., Bergeman, T., & DeMille, D. (2005). Optical production of ultracold polar molecules. *Physical Review Letters, 94*, 203001.

Sagle, J., Namiotka, R. K., & Huennekens, J. (1996). Measurement and modelling of intensity dependent absorption and transit relaxation on the cesium D_1 line. *Journal of Physics B – Atomic Molecular and Optical Physics, 29*, 2629–2643.

Salihoglu, O., Qi, P., Ahmed, E. H., Kotochigova, S., Magnier, S., & Lyyra, A. M. (2008). Comparison of Autler–Townes splitting based absolute measurements of the $^7Li_2$ $A^1\Sigma_u^+$–$X^1\Sigma_g^+$ electronic transition dipole moment with ab initio theory. *Journal of Chemical Physics, 129*, 174301.

Santori, C., Tamarat, P., Neumann, P., Wrachtrup, J., Fattal, D., Beausoleil, R. G., Rabeau, J., Olivero, P., Greentree, A. D., Prawer, S., Jelezko, F., & Hemmer, P. (2006). Coherent population trapping of single spins in diamond under optical excitation. *Physical Review Letters, 97*, 247401.

Schempp, H., Guenter, G., Hofmann, C. S., Giese, C., Saliba, S. D., Depaola, B. D., Amthor, T., Weidemueller, M., Sevincli, S., & Pohl, T. (2010). Coherent population trapping with controlled interparticle interactions. *Physical Review Letters, 104*, 173602.

Scully, M. O., & Zubairy, M. S. (1997). *Quantum optics*. Cambridge: Cambridge University Press.

Sevincli, S., Ates, C., Pohl, T., Schempp, H., Hofmann, C. S., Guenter, G., Amthor, T., Weidemueller, M., Pritchard, J. D., Maxwell, D., Gauguet, A., Weatherill, K. J., Jones, M. P. A., & Adams, C. S. (2011). Quantum interference in interacting three-level Rydberg gases: Coherent population trapping and electromagnetically induced transparency. *Journal of Physics B – Atomic Molecular and Optical Physics, 44*, 184018.

Shore, B. W. (1990). *The theory of coherent atomic excitation*. New York: Wiley.

Sillanpää, M. A., Li, J., Cicak, K., Altomare, F., Park, J. I., Simmonds, R. W., Paraoanu, G. S., & Hakonen, P. J. (2009). Autler–Townes effect in a superconducting three-level system. *Physical Review Letters, 103*, 193601.

Skinner, D. R., & Whitcher, R. E. (1972). Measurement of the radius of a high power laser beam near the focus of a lens. *Journal of Physics E – Scientific Instruments, 5*, 237–238.

Spano, F. C. (2001). Theory of sub-doppler Autler–Townes splitting in molecules: Alignment and orientation of the angular momentum in nonpolar molecules. *Journal of Chemical Physics, 114*, 276–288.

Stair, R., Schneider, W. E., & Jackson, J. K. (1963). A new standard of spectral irradiance. *Applied Optics, 2*, 1151–1154.

Stenholm, S. (1984). *Foundations of laser spectroscopy*. New York: Wiley Interscience.

Stolte, S. (1988). *Atomic and molecular beam methods*. New York: Oxford University Press.

Sun, H. Q., & Huennekens, J. (1992). Spin–orbit perturbations between the $A(2)^1\Sigma^+$ and $b(1)^3\Pi_0$ states of NaK. *Journal of Chemical Physics, 97*, 4714–4722.

Sussman, B. J., Ivanov, M. Y., & Stolow, A. (2005). Nonperturbative quantum control via the nonresonant dynamic Stark effect. *Physical Review A, 71*, 051401.

Sussman, B. J., Underwood, J. G., Lausten, R., Ivanov, M. Y., & Stolow, A. (2006). Quantum control via the dynamic Stark effect: Application to switched rotational wave packets and molecular axis alignment. *Physical Review A, 73*, 053403.

Sweeney, S. J., Ahmed, E. H., Qi, P., Kirova, T., Lyyra, A. M., & Huennekens, J. (2008). Measurement of absolute transition dipole moment functions of the $3^1\Pi \rightarrow 1(X)^1\Sigma^+$ and $3^1\Pi \rightarrow 2(A)^1\Sigma^+$ transitions in NaK using Autler–Townes spectroscopy and calibrated fluorescence. *Journal of Chemical Physics, 129*, 154303.

Tellinghuisen, J. (1984). Reflection and interference structure in diatomic Franck–Condon distributions. *Journal of Molecular Spectroscopy, 103*, 455–465.

Tellinghuisen, J. (1985). The Franck-Condon principle in bound-free transitions *in Photodissociation and photoionization*, Lawley, K.P. (Ed.). New York: John Wiley & Sons.

Turukhin, A. V., Sudarshanam, V. S., Shahriar, M. S., Musser, J. A., Ham, B. S., & Hemmer, P. R. (2002). Observation of ultraslow and stored light pulses in a solid. *Physical Review Letters, 88*, 023602.

Underwood, J. G., Spanner, M., Ivanov, M. Y., Mottershead, J., Sussman, B. J., & Stolow, A. (2003). Switched wave packets: A route to nonperturbative quantum control. *Physical Review Letters, 90*, 223001.

Vamivakas, A. N., Zhao, Y., Lu, C. -Y., & Atatuere, M. (2009). Spin-resolved quantum-dot resonance fluorescence. *Nature Physics, 5*, 198–202.

Vitanov, N. V., Fleischhauer, M., Shore, B. W., & Bergmann, K. (2001). Coherent manipulation of atoms and molecules by sequential laser pulses. *Advances in Atomic, Molecular, and Optical Physics, 46*, 55–190.

Viteau, M., Chotia, A., Allegrini, M., Bouloufa, N., Dulieu, O., Comparat, D., & Pillet, P. (2008). Optical pumping and vibrational cooling of molecules. *Science, 321*, 232–234.

Voigt, A. C., Taglieber, M., Costa, L., Aoki, T., Wieser, W., Hansch, T. W., & Dieckmann, K. (2009). Ultracold heteronuclear Fermi–Fermi molecules. *Physical Review Letters, 102*, 020405.

Wang, J., Kong, L. B., Tu, X. H., Jiang, K. J., Li, K., Xiong, H. W., Zhu, Y. F., & Zhan, M. S. (2004). Electromagnetically induced transparency in multi-level cascade scheme of cold rubidium atoms. *Physics Letters A, 328*, 437–443.

Weiner, J., & Ho, P. -T. (2003). *Light-matter interaction*. Hoboken, New Jersey: John Wiley & Sons.

Wollenhaupt, M., Liese, D., Prakelt, A., Sarpe-Tudoran, C., & Baumert, T. (2006a). Quantum control by ultrafast dressed states tailoring. *Chemical Physics Letters, 419*, 184–190.

Wollenhaupt, M., Prakelt, A., Sarpe-Tudoran, C., Liese, D., & Baumert, T. (2005). Strong field quantum control by selective population of dressed states. *Journal of Optics B – Quantum and Semiclassical Optics, 7*, S270–S276.

Wollenhaupt, M., Prakelt, A., Sarpe-Tudoran, C., Liese, D., Bayer, T., & Baumert, T. (2006b). Femtosecond strong-field quantum control with sinusoidally phase-modulated pulses. *Physical Review A, 73*, 063409.

Wu, M., Bemish, R. J., & Miller, R. E. (1994). Photodissociation of molecules oriented by DC electric fields: Determining photofragment angular distributions. *Journal of Chemical Physics, 101*, 9447–9456.

Xie, X. B., & Field, R. W. (1985). The $^6Li_2$ $A^1\Sigma_u^+ \sim b^3\Pi_u$ spin orbit perturbations: Sub-Doppler spectra and steady-state kinetic lineshape model. *Chemical Physics, 99*, 337–345.

Xu, S., Sha, G. H., Jiang, B., Sun, W. Z., Chen, X. L., & Zhang, C. H. (1994). Two-color study of Autler–Townes doublet splitting and AC Stark shift in multiphoton ionization spectra of CO. *Journal of Chemical Physics, 100*, 6122–6124.

Xu, X., Sun, B., Berman, P. R., Steel, D. G., Bracker, A. S., Gammon, D., & Sham, L. J. (2007). Coherent optical spectroscopy of a strongly driven quantum dot. *Science, 317*, 929–932.

Xu, X. D., Sun, B., Berman, P. R., Steel, D. G., Bracker, A. S., Gammon, D., & Sham, L. J. (2008). Coherent population trapping of an electron spin in a single negatively charged quantum dot. *Nature Physics, 4*, 692–695.

Yi, P., Song, M., Liu, Y. M., Field, R. W., Li, L., & Lyyra, A. M. (2004). Experimental observation of Autler–Townes splitting of the Na_2 $A^1\Sigma_u^+ \sim b^3\Pi_u$ mixed levels. *Optics Communications, 233*, 131–138.

Yiannopoulou, A., Ji, B., Li, L., Li, M., Urbanski, K., Lyyra, A. M., Stwalley, W. C., & Jeung, G. H. (1994). The doubly excited $1^3\Sigma_g^-$ state of $^7Li_2$. *Journal of Chemical Physics, 101*, 3581–3587.

Zwierlein, M. W., Stan, C. A., Schunck, C. H., Raupach, S. M. F., Gupta, S., Hadzibabic, Z., & Ketterle, W. (2003). Observation of Bose–Einstein condensation of molecules. *Physical Review Letters, 91*, 250401.